A comprehensive study on the treatment of various organic pollutants by NiCoFe layered double oxide: material synthesis and characterization, decomposition mechanism exploration, and real water applications

Nguyen Trung Dung[1,*], Nguyen Hoang Duc[1], Vi Thai Binh[1], Vu Dinh Thao[1], Manh B. Nguyen[2], Le Viet Ngan[3], Nguyen Nhat Huy[4,5,*]

[1] *Faculty of Physical and Chemical Engineering, Le Quy Don Technical University, 236 Hoang Quoc Viet St., Bac Tu Liem District, Hanoi, Vietnam*

[2] *Institute of Chemistry (IOC), Vietnam Academy of Science and Technology (VAST), 18 Hoang Quoc Viet, Cau Giay, Hanoi, Viet Nam*

[3] *National Institute for Food Control, 65 Pham Than Duat Street, Mai Dich Ward, Cau Giay District, Hanoi, Vietnam*

[4] *Faculty of Environment and Natural Resources, Ho Chi Minh City University of Technology (HCMUT), 268 Ly Thuong Kiet Street, District 10, Ho Chi Minh City, Vietnam*

[5] *Vietnam National University Ho Chi Minh City, Linh Trung Ward, Thu Duc City, Ho Chi Minh City, Vietnam*

Submitted to

Separation and Purification Technology

* Corresponding authors:

- Dr. Nguyen Trung Dung, Faculty of Physical and Chemical Engineering, Le Quy Don Technical University, 236 Hoang Quoc Viet St., Bac Tu Liem Dist., Hanoi, Vietnam. Tel: +84 968 368 305. Email: ntdung@lqdtu.edu.vn
- Assoc. Prof. Nguyen Nhat Huy, Faculty of Environment and Natural Resources, Ho Chi Minh City University of Technology (HCMUT), 268 Ly Thuong Kiet St., Dist. 10, Ho Chi Minh City, Vietnam. Tel: +84 901 964 985. Email: nnhuy@hcmut.edu.vn

Abstract

In this report, we successfully synthesized NiCoFe layered double oxide (NiCoFe-LDO) by heating a hydrothermally prepared NiCoFe layered double hydroxide in the air at 400-700 °C. The morphology, crystal structure, surface area, elemental composition and environment, functional groups, thermal stability, and magnetic properties of the materials were determined by SEM, XRD, BET, XPS, FTIR, TGA-DTG, and VSM analyses. The material was then used to activate potassium peroxymonosulfate (PMS) for degrading Rhodamine B (RhB) other dyes in different conditions of water, surface water, and wastewater. The results showed that NiCoFe-LDO annealed at 500 °C can remove 97.86% RhB (20 mg/L) in 14 min at pH 7. Moreover, the presence of anions (i.e., HPO_4^-, HCO_3^-, CO_3^{2-}, NO_3^-, Cl^-, and SO_4^{2-}) in the solution affected the RhB removal efficiency. In various dyes removal tests, the removal efficiency of the dyes was in the order of RhB > OG > DB71 ≈ MO ≈ TTZ ≈ JGB ≈ MB. In the radical scavenging tests, the occurrence and role of radicals in RhB degradation were in the order of $O_2^{\bullet-}$ > $^1O_2$ > $SO_4^{\bullet-}$ > $HO^{\bullet}$, thus the degradation of RhB is based on both radical and nonradical reactions. Moreover, the intermediates formed during the reaction were detected. Accordingly, the mechanism of RhB degradation by the NiCoFe-LDO under PMS activation was proposed. Finally, the durability of the materials and its high dyes and organics removal efficiency in both surface water and actual wastewater suggests a great potential for practical applications of NiCoFe-LDO/PMS in wastewater treatment, especially for the recalcitrant components.

Keywords: peroxymonosulfate, NiCoFe-LDO, dyes, wastewater treatment, reactive oxygen species

1. Introduction

Organic dyes discharged from the printing, textile, and dyeing industries have adverse effects on the environment, characterized by their high color, COD, and pH. This prevents the penetration of sunlight and affects aquatic life by reducing dissolved oxygen [1-3]. Therefore, the development of treatment methods to remove dyes from wastewater is urgently required. Several procedures have been used to solve this problem such as coagulation/flocculation [4], activated carbon adsorption [5], membrane technology [6], and advanced oxidation processes (AOPs) [2, 7]. Among them, AOPs based on potassium peroxymonosulfate (PMS) are considered the prospective method to decomposition organics pollutions in water by high oxidizing ability. The reactive oxygen species such as sulfate ($SO_4^{\bullet-}$), hydroxyl ($^{\bullet}OH$), superoxide ($O_2^{\bullet-}$), and singlet oxygen ($^1O_2$) can be formed directly from the activation of PMS by heterogeneous catalysts. They are potential oxidizing agents that can decompose organic pollutants into low toxicity intermediates or even mineralized products of H_2O and CO_2 [8-10]. Compared with hydroperoxide and persulfate, the activation of peroxymonosulfate by heterogeneous catalyst has many advantages such as asymmetric structure, low activation energy, wide pH range (instead of at pH = 3 for H_2O_2) with a O - O distance of 1.453 Å and a binding energy in the range 140-213.3 kJ/mol [9, 11, 12].

On the other hand, layered double hydroxide (LDH), also known as hydrotalcite, is a synthetic clay-like material with a special layered structure and variation of metal ions in the sheet, which create a great catalytic potential for contaminant removal. The general formula for LDHs is $[M^{2+}_{1-x}M^{3+}_x(OH)_2]^{x+}[(A^{n-})_{x/n-}]^{x-}.mH_2O$. Regarding cations, M^{3+} is a trivalent metal cation (e.g., Al, Cr, and Fe) and M^{2+} is a divalent metal cation (e.g., Mg, Ni, and Co). Regarding anion, A^{n-} can be an anion (e.g., halogen, or SO_4^{2-}, CO_3^{2-}, and HO^-) anion complex, organics anion, high-molecular-weight polymer, and x is the $M^{3+}/(M^{2+} + M^{3+})$ atomic ratio with $0.1 < x < 0.5$ [13-17]. After being heated at a high temperature in the air, the alternating anions of LDH can be eliminated, resulting

in the annealed products of LDH as layer double oxide (LDO) retaining the original layered structure of LDH. LDO has a large specific surface area and porosity, excellent metal oxide dispersion, and is more stable than the corresponding LDH, thus it has the potential to be used as a catalyst more widely than LDH [18-20]. Besides, LDOs prepared from LDH precursors have advantages over metal oxide mixtures (i.e., metal mixed oxide, MO) because they tend to be more homogeneous due to the insertion of divalent and trivalent metals into brucite layers [9, 21]. Using LDO as a heterogeneous catalyst to activate PMS has many advantages such as no energy input, reusability of the catalyst, and limited secondary pollution of dissolved metals. Recently, there have been several publications on the synthesis of secondary and tertiary LDOs that activate PMS to degrade organic pollutants in water such as CoAl-LDO for RhB [22], CoMgAl-LDO for atrazine [23], CoCuAl-LDO for orange acid 7 [24], CoMgFe-LDO for carbamazepine [25], CoMnAl-LDO for bisphenol A [26], and CuCoFe-LDO for p-nitrophenol [27]. Compared to other transition metals, the Ni^{2+}, Co^{2+}, and Fe^{2+} ions are more favorable for redox properties and could be highly catalytically effective for PMS activation for organic pollutant degradation. However, to the best of our knowledge, there has not been any study on the synthesis of NiCoFe-LDO for PMS activation and dyes treatment in both synthetic and actual water/wastewater.

In this study, NiCoFe-LDO was synthesized from NiCoFe-LDH precursor to activate PMS for dye removal. The crystalline structure and morphological characteristics of NiCoFe-LDO were characterized by several surface analysis techniques. The influence of some factors such as annealing temperature, catalyst system, catalyst dosage, PMS and Rhodamine B concentration, and solution pH on the decomposition of Rhodamine B was investigated. In addition, the stability, as well as the reusability of the catalyst, was also studied. The reactive oxygen species formed in

the NiCoFe-LDO/PMS system were determined and the reaction mechanism is also proposed. The tests with various dyes, surface waters, and wastewaters were also conducted.

2. Materials and methods

2.1. Synthesis and characterizations of the material

Chemicals used for material synthesis in this study include cobalt (II) nitrate hexahydrate ($Co(NO_3)_2.6H_2O$), nickel (II) nitrate hexahydrate ($Ni(NO_3)_2.6H_2O$), potassium peroxymonosulfate (PMS), iron (III) nitrate ($Fe(NO_3)_3.9H_2O$), urea ($(NH_2)_2CO$), and double-distilled water. Other chemicals for running experiments and analysis were $NaNO_3$, NaCl, Na_2SO_3, Na_2HPO_4, Na_2CO_3, $NaHCO_3$, $C_{28}H_{31}ClN_2O_3$ (Rhodamine B or RhB), Orange G (OG), Direct Blue 71 (DB71), Methyl Orange (MO), Tartrazine (TTZ), Janus Green B (JGB), Methylene Blue (MB), C_2H_5OH, C_6H_5OH (phenol or PheOH), C_4H_9OH (tert-butyl alcohol or TBA), $C_5H_6O_2$ (furfuryl alcohol or FFA), and $C_6H_4O_2$ (p-Benzoquinone or p-BQ), 5,5-dimethyl-1-pyrroline-N-oxide (DMPO), and 2,2,6,6-tetramethylpiperidine (TEMP). All of them are in pure form bought from China and are intended for direct use without any further treatment.

NiCoFe-LDH was synthesized by a hydrothermal method. A mixture of 2.5 mmol $Ni(NO_3)_2.6H_2O$, 7.5 mmol of $Co(NO_3)_2.6H_2O$, 5 mmol of $Fe(NO_3)_3.9H_2O$, and 3 g of urea was mixed and completely dissolved in 50 mL of ethanol after 30 min. The solution was then transferred into an autoclave and hydrothermally treated at 120 °C for 12 h (Fig. S1 of Supplementary Material). After that, the suspension was filtered and washed several times with ethanol and double distilled water to pH 7. The material was subsequently dried at 60 °C for 12 h to yield a brown NiCoFe-LDH powder. Next, the powder was heated in air at a temperature of 400-700 °C at a heating rate of 2 °C/min to yield a black color material named as NiCoFe-LDOx, where x is the calcination

temperature. Other materials such as NiCo-LDO, CoFe-LDO, and NiFe-LDO were synthesized under the same conditions without adding a third element in the material synthesis procedure.

The morphology and surface elemental composition of the synthesized materials were analyzed by scanning electron microscopy (SEM, S-4800, Hitachi) coupling with energy-dispersive X-ray spectroscopy (EDX). The crystalline structure was examined through X-ray diffraction (XRD, X'Pert PRO, Philips). The surface chemistry and functional groups were investigated by Fourier-transform infrared spectroscopy (FTIR, Spectrum Two, Perkin Elmer). The Brunauer–Emmett–Teller (BET) adsorption-desorption method was used to determine the surface area and pore size distribution of the material using a surface area and porosity analyzer (TriStar II Plus 2.03, Micromeritics). Thermal gravimetric analysis (TGA) was used to study the thermal transformation and the stability of the material. The chemical environment was studied by X-ray photoelectron spectroscopy (XPS, VG Multilab 2000, Thermo Fisher Scientific). The magnetic properties of the synthesized materials were examined by a vibrating sample magnetometer equipped with a 1 T magnet (MicroMag 3900 model, PMC). The composition and weight of metals in the NiCoFe-LDO material samples before and after the reaction were analyzed by ICP-MS 7900 Instrument (Agilent, USA) with analytical conditions: Argon gas flow rate of 15 L/min, carrier gas flow of 1 L/min, auxiliary gas flow of 0.5 L/min, Helium measurement mode, and 1500W RF energy. The intermediates of RhB degradation were detected by MS (Waters, USA) with electrospray positive ion (ESI+) mode. The MS conditions were as follows: capillary voltage of 3.47 kV, cone voltage of 115 V, source temperature and desolvation temperature of 150 °C and 200 °C, respectively, and in the positive mode. The scanning range was in the m/z range from 0 to 600 with a flow rate of 20 µL/min.

The reactive oxygen species was identified by electron paramagnetic resonance spectroscopy (EPR, Bruker 300, Germany) using DMPO and TEMP as spin trapping agents. The operating conditions were as follows: center field of 3300 G, sweep width of 1000 G, microwave frequency of 14.5 GHz, modulation frequency of 100 kHz, and microwave power of 6 mW. The detection of $^1O_2$ was conducted in water solution while the detection of $O_2^{\bullet-}$ was carried out in ethanol solution.

The chemical oxygen demand (COD) of the sample was measured by the method of SMEWW 5220B:2017. The point of zero charge (pH_{pzc}) of the material was determined by the titration method at the pH point that was not change after adding of material in a solution of NaCl 0.1 M with different initial pH values.

2.2. Catalytic activation experiments

The NiCoFe-LDO stock suspension with a concentration of 1000 mg/L and the PMS stock solution of 5000 mg/L were prepared daily by weighing an exact amount of the material/chemical and then dispersed/dissolved in a volumetric flask with double distilled water. The RhB stock solution of 1000 mg/L was also prepared and the RhB working solution of 100 mg/L RhB was prepared by diluting from the stock RhB solution.

The catalytic activation was performed as follows. A 5-mL volumetric flask containing 1 mL of 100 mg/L RhB was added with 0.3 mL of 1000 mg/L NiCoFe-LDO suspension, shaken for 30 min for reaching adsorption-desorption equilibrium. The mixture was then added with 0.5 mL of 5000 mg/L PMS solution, filled with double distilled water, and continuously shaken during the test. In the test for investigating the effects of temperature, the tested volume is increased by 100 times and put in a beaker containing water heated at different temperatures. At certain periods, 4 mL of water samples were taken and added with 0.2 mL of 0.1 M Na_2SO_3 solution to stop the oxidation process by radicals before sending for RhB concentration measurement at 554 nm using a UV-visible spectrophotometer (Libra S60, Biochrom, UK). In the test of anion effects, solutions

containing Cl^-, CO_3^{2-}, HCO_3^-, HPO_4^{2-}, NO_3^-, and SO_4^{2-} were added at a concentration ranging from 1 to 10 mM. The role of radicals was tested by adding quenching agents such as FFA, EtOH, TBA, IPA, PheOH, and p-BQ with a concentration of 1 mM to the RhB solution before adding PMS solution. The study also conducted experiments using water from rivers and lakes to investigate the applicability of the technology in practice. Ảnh hưởng của nền trong các mẫu nước mặt đến sự loại bỏ RhB đã được khảo sát. Các mẫu nước mặt được thu thập từ các sông và hồ (Hà Nội, Việt Nam).

3. Results and discussion

3.1. Material characterizations

The SEM images of the NiCoFe-LDH and NiCoFe-LDO prepared at different annealing temperatures are displayed in Fig. 1. NiCoFe-LDH shows flower-like spheres with needles of various lengths on the surfaces. In addition, the surface structure of the material is relatively uniform and highly ordered. After being heated at 500-700 °C, the needles gradually transform into nanofibers, nanorods, and nanoparticles, thus reducing the porosity but still keeping the original spherical structure. The diameter of the needles in NiCoFe-LDH was estimated at 30-50 nm. The diameters/sizes of the NiCoFe-LDO fibers (at 500 °C), rods (at 600 °C), and particles (at 700 °C) were estimated to be 30-50, 50-100, and 70-200 nm, respectively. EDX result of NiCoFe-LDO material annealed at 500 °C is presented in Fig. S2, showing the main component of Ni, Co, Fe, and O elements and proving that the material was successfully synthesized and of high purity. On the other hand, the analysis results of the Ni, Co, and Fe elements by ICP-MS method showed that the percentage of Ni, Co, and Fe elements were 1.86, 16.44, and 14.45% ở 500^{o}C, 3.72, 11.29 and 24.37% ở 600^{o}C, 5.85, 10.36 and 27.04% ở 700^{o}C, respectively. Như vậy, ở nhiệt độ 500^{o}C, hàm lượng nguyên tố Ni trong vật liệu NiCoFe-LDO 500 thấp (1.86%), không quan sát sự hình

184 thành pha $NiFe_2O_4$ ở nhiệt độ này. Tuy nhiê, khi nhiệt độ tăng hàm lượng Ni và Fe có xu hướng
185 tăng, đồng thời hàm lượng của Co giảm, điều đó phù hợp với kết quả phân tích phổ nhiễu xạ tia X
186 sự hình thành pha $NiFe_2O_4$ ở nhiệt độ cao, kết quả này cũng phù hợp với công bố của P.D. Patil và
187 cộng sự [https://doi.org/10.1016/j.est.2021.102821].

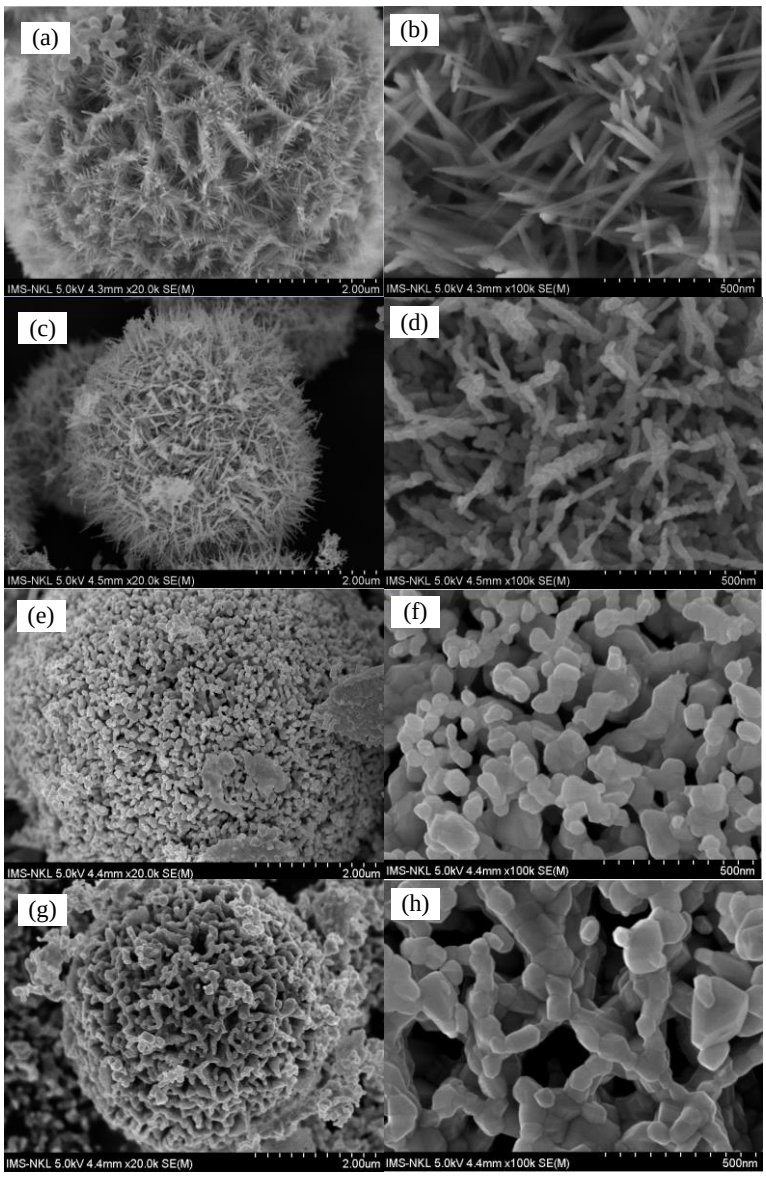

Fig. 1. SEM images of (a, b) NiCoFe-LDH, and NiCoFe-LDO synthesized at (c, d) 500, (e, f) 600, and (g, h) 700 ^{o}C

The XRD patterns of the synthesized materials are shown in Fig. 2(a). NiCoFe-LDH material is a typical layered double hydroxide structure with peaks at 2θ of 12.64, 25.26, and 32.66°, corresponding to the planes of (003), (006), and (012), respectively [28], proving that the material was successfully synthesized. Cơ chế hình thành NiCoFe-LDH có thể được giải thích như sau: Đầu tiên, ethanol sẽ trải qua quá trình ete hóa (phản ứng 1) tạo ra một lượng nhỏ nước, lượng nước này cùng với nước trong tinh thể của các tiền chất muối nitrat sẽ hỗ trợ quá trình thủy phân urê để tạo thành amoni cacbonat, như được minh họa trong các phản ứng 2 và 3. Tiếp theo, sự thủy phân của cacbonat sẽ tạo ra lượng nhỏ ion hydroxyl [DOI 10.1007/s12274-016-1197-4]. Do tích số tan của $Fe(OH)_3$ ($K_{sp}=4.0\times10^{-38}$) thấp hơn rất nhiều so với $Ni(OH)_2$ ($K_{sp}=1.58\times10^{-15}$) và $Co(OH)_2$ ($K_{sp}=2.0\times10^{-15}$), vì vậy Fe^{3+} ưu tiên hình thành ở dạng $Fe(OH)_3$, trong khi Ni^{2+} và Co^{2+} ưu tiên hình thành ở dạng kết tủa cacbonat [DOI 10.1007/s12274-016-1197-4; https://doi.org/10.1016/j.electacta.2017.10.074]. Sự hình thành tinh thể NiCoFe-LDH trải qua một số bước như hình thành các bảng nano LDH 2D bằng quá trình tăng trưởng tinh thể. Khi phản ứng kéo dài, các bảng nano LDH 2D tự lắp ráp thành các vi cầu 3D giống như bông hoa với sự phân cấp cấu trúc xốp. Ở đây, có nhiều lực lượng tham gia xây dựng cấu trúc độc đáo này, bao gồm tĩnh điện, tương tác mặt tinh thể, liên kết hydro và van der Waals. Do ethanol là dung môi phân cực, vai trò của nó thể hiện ở chỗ có thể thay đổi năng lượng bề mặt của tinh thể, làm giảm tốc độ tăng trưởng của tinh thể do các đặc tính độc đáo của nó như như nhiệt độ sôi cao, khả và tương đối mạnh cực. Điều đó dẫn đến sự hình thành cấu trúc vi cầu hoa [10.1016/j.jallcom.2016.11.419]

Chúng tôi tính toán được giá trị d003 của NiCoFe-LDH tổng hợp bằng phương pháp thủy nhiệt trong môi ethanol là 0,7nm bé hơn so với giá trị d003 của NiCoFe-LDH tổng hợp bằng phương pháp thủy nhiệt trong dung môi nước hoặc đồng kết tủa (0,79nm) [https://doi.org/10.1016/j.electacta.2017.10.074], cấu trúc NiCoFe-LDH bị thu gọn có thể được tạo ra bởi sự thiếu nước trong lớp xen kẽ. NiCoFe-LDH tổng hợp bằng phương pháp thủy nhiệt trong ethanol có giá trị 2θ của đỉnh đặc trưng 003 (12,64) được chuyển sang lớn hơn đáng kể so với giá trị 2θ truyền thống (11,76), điều này được giải thích bởi sự giảm khoảng cách giữa các lớp (d003).

$$2CH_3CH_2OH \rightarrow C_2H_5OC_2H_5 + H_2O \quad (1)$$

$$CO(NH_2)_2 \rightarrow NH_4CNO \quad (2)$$

$$CO(NH_2)_2 + 2H_2O \rightarrow 2NH_4^+ + CO_3^{2-} \quad (3)$$

$$CO_3^{2-} + H_2O \rightarrow HCO_3^- + OH^- \quad (4)$$

$$Ni^{2+} + 3Co^{2+}\ 2Fe^{3+} + 6OH^- + 6CNO^- + 0.165CO_3^{2-} \rightarrow 6[Ni_{0.165}Co_{0.505}Fe_{0.33}(OH)(CNO)]^{0.33+}[(CO_3^{2-})_{0.165}.mH_2O] \quad (5)$$

After annealing at 500-700 °C, the layered structure was corrupted while the spinel structures appeared. Specifically, the trivalent cations in the brucite structure diffuse into the anion interlayer space, accompanied by the dehydration and elimination of the interlayer anion. Whereas trivalent cations move from octahedral to tetrahedral, divalent cations remain in octahedral. Then, trivalent cations in the interlayer space and divalent cations in the layered plate can form spinel oxide [24].

In NiCoFe-LDO material calcined at 400 ^{o}C, the peak at 2θ of 12.64^{o} was found for NiCoFe-LDH structure. The characteristic peaks at 2θ of 18.93, 31.24, 36.72, 38.56, 44.83, 55.68, 59.23, and 65.08° were observed for Co_3O_4 (JCPDS 43-1003), at 2θ of 18.34, 30.22, 35.65, 43.30, 57.24 and 63.00^{o} for Fe_3O_4 (JCPDS 75-1609), and 24.35, 33.19, 49.54, 54.10, and 74.32° for Fe_2O_3 (JCPDS 33-0664). These indicate that the low temperature of 400 ^{o}C was not sufficient for the complete transformation of NiCoFe-LDH into NiCoFe-LDO. Moreover, the diffraction peak intensities of Co_3O_4 are higher than those of Fe_3O_4.

After being calcined at 500 °C, characteristic peaks were observed for Co_3O_4 (JCPDS 43-1003) at 2θ of 18.93, 31.24, 36.72, 44.83, 55.68, 59.23, and 65.08°; for Fe_3O_4 (JCPDS 75-1609) at 2θ of 18.34, 30.22, 35.65, 43.30, 57.24, and 63.00°; and for Fe_2O_3 (JCPDS 33-0664) at 2θ of 24.35, 33.19, 49.54, 54.10, and 74.32°. The diffraction peak intensities of Co_3O_4 are similar to those of Fe_3O_4, improving the magnetic property of the material. Noticeably, no characteristic diffraction peaks of nickel compounds were observed, possibly due to the low content of Ni in the catalyst. In addition, it is also possible that at 400-500 °C, the nickel compounds exist in amorphous form and are highly dispersed in the crystal lattice of the spinel. After annealing of 600°C and 700^{o}C, the characteristic peaks of the NiCoFe-LDO material were observed for Co_3O_4 (18.93, 31.24, 36.72, 44.83, 55.68, 59.23, and 65.08°), $NiFe_2O_4$ (JCPDS 44-1485, at 18.28, 30.21, 35.53, 43.21, 57.13, and 62.80^{o}) and Fe_2O_3 (24.35, 33.19, 54.10, and 74.32^{o}). Finally, NiCoFe-LDO annealed at 700 °C has characteristic peaks of Co_3O_4 (18.93, 31.24, 36.72, 44.83, 55.68, 59.23, and 65.08°) and $NiFe_2O_4$ (18.28, 30.21, 35.53, 43.21, 53.47, 57.13, 62.80, and 74.20°). Therefore, when increasing the annealing temperature from 500 to 700 °C, the diffraction intensity of Co_3O_4 tends to decrease while the diffraction intensity of $NiFe_2O_4$ increases, cực đại nhiễu xạ của $NiFe_2O_4$ trở nên hẹp và sắc nét hơn khi tăng nhiệt độ nung [https://doi.org/10.1016/j.est.2021.102821], kích thước tinh thể trung bình của $NiFe_2O_4$ tại giá trị 2θ= 35.53^{o} ở nhiệt độ 600 và 700^{o}C theo công thức Debye – Scherrer (Phương trình 1) là 73.2 và 28.1 nm tương ứng.

Commented [D1]: Bỏ đoạn này

$$D = \frac{0.9\lambda}{\beta \cos\theta}$$

trong đó, trong đó λ, β, θ là bước sóng tia X, chiều rộng toàn phần bằng một nửa

cực đại (FWHM) của đỉnh nhiễu xạ và góc nhiễu xạ Bragg tương ứng. At 600 °C, no Fe_3O_4 phase was observed while at 700 °C, the Fe_2O_3 phase was not detected. Since the radius of Ni(II) (0.72 Å) and Ni(III) (0.62 Å) are smaller than those of Fe(II) (0.76 Å) and Fe(III) (0.64 Å), a part of Ni(II) and Ni(III) could be inserted into the lattice of Fe_3O_4 or Fe_2O_3 to form a $NiFe_2O_4$ solid solution at high annealing temperatures of 600-700 °C. In brief, there was a gradual increase in the crystalline structure of the materials with the increase of calcination, where the LDH structure almost completely transforms into an LDO structure at a calcination temperature of 500 ^oC.

The FTIR spectra of NiCoFe-LDH and NiCoFe-LDO prepared at temperatures of 400-700 °C are plotted in Fig. 2(b). NiCoFe-LDH shows a broad absorption peak at a wavenumber of 3480 cm^{-1}, possibly due to the stretching vibration of OH groups in water molecules of the interlayer. The peak appearance at 2148 cm^{-1} characterizes the absorption band of OCN- formed from urea degradation by-products [28]. The peaks at 1380 and 1316 cm^{-1} are attributed to the deformation of the water molecules and the asymmetric stretching vibration of the carbonate anion in the interlayer [29]. Furthermore, the peaks in the range of 400-1000 cm^{-1} are attributed to metal-oxygen (M-O) and metal-hydroxyl (M-OH) bonds. The combination of XRD and FTIR results shows that the NiCoFe-LDH material was successfully synthesized. In NiCoFe-LDO materials, the bands at 1380 and 1316 cm^{-1} almost disappeared, suggesting the destruction of the anion layer interspersed with CO_3^{2-} after being annealed at 400-700 °C. Furthermore, the band observed near 659 and 533 cm^{-1} is specific for the M-O bond. The XRD and FTIR results indicated that the annealing at 500-700 °C destroyed the structure of LDH and transform it into the new form of LDO structure.

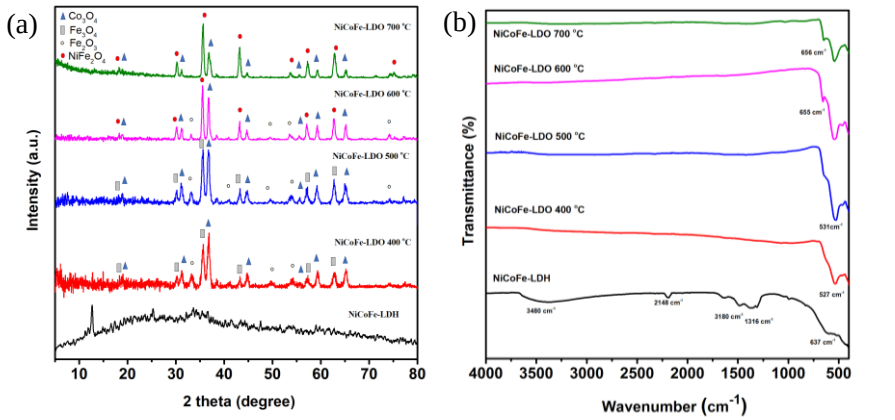

277

278 Fig. 2. (a) XRD patterns and (b) FTIR spectra of NiCoFe-LDH and NiCoFe-LDO prepared at

279 different temperatures

280 The N_2 adsorption-desorption isotherms of NiCoFe-LDO and the pore sizes at different annealing

281 temperatures are demonstrated in Fig. S3. All NiCoFe-LDO materials display type IV isotherm

282 characteristics with an H3 hysteresis loop (IUPAC classification). These types represent a structure

283 of narrow parallel walls, bottle-neck, or aggregates of uniform particles. NiCoFe-LDH and

284 NiCoFe-LDO materials prepared at 400, 500, 600, and 700 ^oC have surface areas of 49.38, 42.27,

285 22.74, 7.86, and 5.15 m^2/g, respectively, pore size of 25.44, 8.70, 24.50, 12.96 and 10.78 nm,

286 respectively, and pore volume of 0.3051, 0.086, 0.156, 0.032, and 0.0234 cm^3/g, respectively

287 (Table S1 of Supplementary Material). The decrease of surface area with the annealing

288 temperature could be due to the larger particle size and more aggregation at higher temperatures.

289 Diện tích bề mặt BET của LDO thấp hơn so với tiền chất LDH, có thể là do trong quá trình nhiệt

290 phân đã làm cho cấu trúc lớp bị sụp đổ và sự co lại trong quá trình nung dẫn đến làm cho thể tích

291 lỗ xốp cũng giảm theo [https://doi.org/10.1016/j.est.2021.102821], điều này được quan sát thấy ở

ảnh SEM của các vật liệu. Besides, the decrease in the surface area of the NiCoFe-LDO materials decreases as compared to NiCoFe-LDH could be due to the large size of Fe^{3+} ion, preventing its transfer from octahedral to the tetrahedral structure and resulted in the low porosity and low surface area of the material [30]. Besides, the decrease in the surface area was also caused by the formation of spinel structure with the increase of calcination temperature, which is consistent with XRD results [31]. Tuy nhiên, với diện tích bề mặt đủ lớn, NiCoFe LDO500 được sử dụng để tăng cường khả năng hấp phụ và cung cấp các vị trí hoạt động trên bề mặt xúc tác để hoạt hóa PMS, hình thành các loại oxy hoạt động, phân ủy chất ô nhiễm hữu cơ trong nước.

The saturation magnetization of the material is an important parameter for determining the magnetic property of the material. As presented in Fig. S4, NiCoFe-LDO 500 material shows very narrow magnetic hysteresis and magnetic coercivity, indicating that NiCoFe-LDO 500 is a superparamagnetic material with a saturation magnetization of 35.13 emu/g. Therefore, the NiCoFe-LDO 500 solid material can be easily collected for reuse from the suspension by applying an external magnetic field. As displayed in the inset of Fig. S4, the NiCoFe-LDO 500 can be readily collected by using a magnet, indicating that this material can be efficiently recovered and recycled for using many times. This reduces the cost of material use and makes it possible for practical application.

The thermal stability of the NiCoFe-LDH material was analyzed by TGA in the temperature range of 50-950 °C and the result is depicted in Fig. S5. In the temperature range from 50-200 °C, the evaporation of adsorbed and interstitial water occurs, leading to a slight mass decrease of 8%. The decomposition of the hydroxide layer of brucite structure occurs in the temperature range of 200-300 ^{o}C with a weight loss of 17%. Next, the process of breaking CO_3^{2-} alternating layers of anion occurs at around > 400 °C to form NiCoFe-LDO oxide and spinel oxide phase, resulting in a slight

mass loss of about 3.82% [32, 33]. In summary, the mass loss can be attributed to the following causes: (i) release of water in the anionic layer and adsorbed water on the surface of the material, (ii) release of hydroxyl groups from brucite-like layers (as water), and (iii) the release of CO_3^{2-} anion between the interlayers.

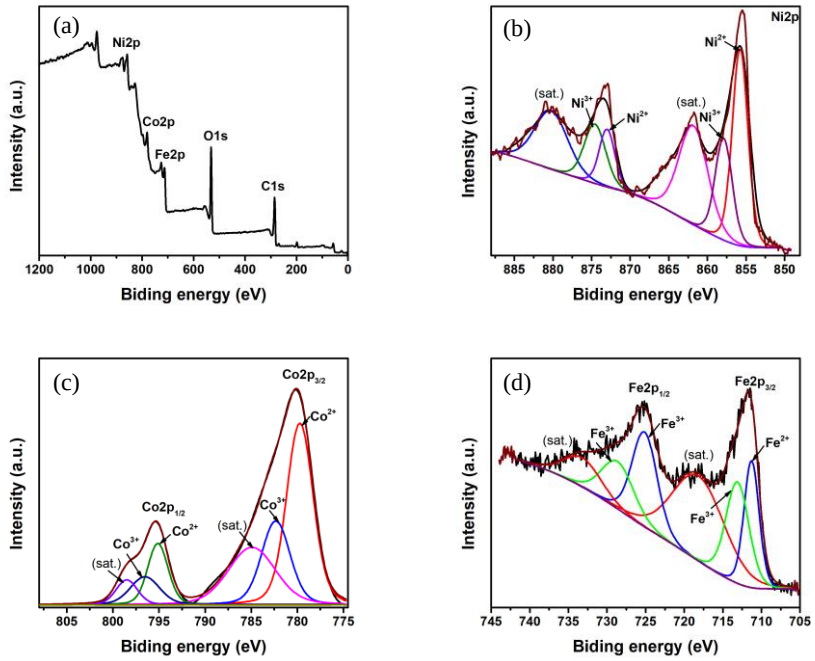

Fig. 3. XPS results of NiCoFe-LDO sample: (a) survey scan, (b) Ni 2p, (c) Co 2p, and (d) Fe 2p

X-ray photoelectron spectroscopy (XPS) was used to analyze the valence state of the NiCoFe-LDO sample. The full-scan XPS spectra of NiCoFe-LDO (Fig. 3(a)) shows the appearance of binding energies at 285.8, 531.9, 711.9, 781.0, and 856 eV, which are assigned to C 1s, O 1s, Fe

2p, Co 2p, and Ni 2p, respectively [34]. The appearance of C 1s at 285.8 eV is due to adventitious hydrocarbon in the XPS instrument [35, 36]. The Ni 2p spectrum (Fig. 3(b)) can be fitted into six peaks. The peaks at 855.8 eV and 872.9 eV are assigned to Ni^{2+}, while peaks at 857.9 and 874.6 eV should be attributed to Ni^{3+} and two shake-up satellites at 855.5 and 875.45 eV (denoted as sat.) [37]. In the Co 2p spectrum (Fig. 3(c)), peaks in the binding energies of Co $2p_{3/2}$ can be attributed to Co^{2+} and Co^{3+} with peak positions at 779.8 and 782.4 eV, respectively, while Co $2p_{1/2}$ peaks can be assigned to Co^{2+} and Co^{3+} with peaks centered at 795.2 and 796.4 eV, respectively [38]. The two shake-up satellites are at 784.9 and 798.4 eV (denoted as sat.) The high-resolution XPS spectra of Fe 2p spectrum (Fig. 3(d)) show two peaks located at 711.2 and 725.3 eV for Fe^{2+}, and two peaks located at 713.2 and 728.8 eV for Fe^{3+} [39].

3.2. Catalytic RhB decomposition

The annealing temperature has a great influence on the morphology, surface chemistry, crystalline structure, and surface area of the material, which in turn affects the active center of the catalyst. Thus it affects the ability to activate PMS, and therefore the formation of reactive oxygen species (e.g., $SO_4^{\bullet-}$, $OH^{\bullet}$, $O_2^{\bullet-}$, and $^1O_2$) for RhB removal. As seen in Fig. 4(a), The RhB decomposition efficiencies by NiCoFe-LDO prepared at 400, 500, 600 and 700 °C were 89.18, 97.86, 93.91, and 90.12%, respectively, after 14 min of reaction, which was much higher than that of NiCoFe-LDH (69.22%). The low efficiency by NiCoFe-LDO prepared at 400 °C could be due to its low crystallinity (as observed from XRD results) since it still contains the LDH structure. The pseudo-first-order reaction rate constant of NiCoFe-LDO prepared at 500 °C had 1.31 and 1.45 higher than those at 600 and 700 ^oC, respectively, and 3.84 times higher than that of NiCoFe-LDH (Fig. S6). The highest efficiency at 500 ^oC can be explained by: (i) the decrease of surface area in the annealing temperature range of 500 °C > 600 °C > 700 ° C leads to the reduction of active sites on

the surface of the catalyst, thereby reducing the ability to activate PMS, and (ii) PMS activation ability of transition metal ions increases in order of $Ni^{2+} < Fe^{3+} < Mn^{2+} < V^{3+} < Ce^{3+} < Fe^{2+} < Ru^{3+} < Co^{2+}$ [40]. Edy Saputra và cộng sự đã chỉ ra khả năng hoạt hóa PMS của Co_3O_4 mạnh hơn Fe_3O4 [http://dx.doi.org/10.1016/j.jcis.2013.06.061], kết quả này cũng được chỉ ra trong nghiên cứu của Hejun Ren [https://doi.org/10.1002/jctb.6498], Liwei Chen [https://doi.org/10.1016/j.cej.2018.11.120]. Among the spinels formed in the NiCoFe-LDO structure, Co_3O_4 can strongly activate PMS. In XRD results, the intensity of the diffraction peak of Co_3O_4 decreased with the increase of annealing temperature from 500 to 700 °C, thus reduces the ability to activate PMS of NiCoFe-LDO catalyst. Therefore, NiCoFe-LDO annealed at 500 °C was chosen for the next studies.

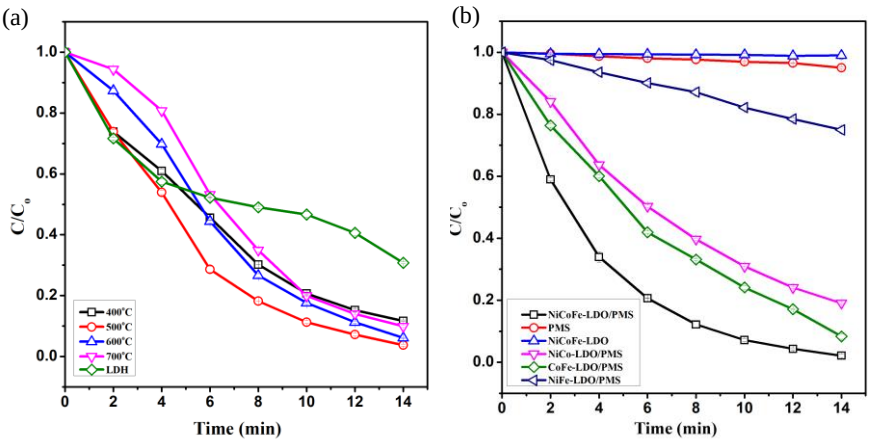

Fig. 4. (a) RhB treatment efficiency of NiCoFe-LDO annealed at different temperatures and (b) RhB treatment efficiency of different reaction systems

(*Condition: 20 mgRhB/L, 500 mgPMS/L, 60 mgLDO/L, pH 7.0, 25 °C*)

Fig. 4(b) demonstrates the performance of different LDO materials for RhB removal. Without PMS, the RhB removal was negligible with only 1.02% after 14 min, showing insignificant adsorption of RhB on the surface of the NiCoFe-LDO catalyst. In the absence of catalyst, the efficiency of RhB removal by PMS was as low as 5% due to the weak oxidizing property of PMS with a redox potential of 1.82 V. In the simultaneous presence of heterogeneous catalyst and PMS, the RhB degradation efficiency increased sharply to 25.07% (NiFe-LDO), 80.94% (NiCo-LDO), 91.68% (CoFe-LDO), and 97.86% (NiCoFe-LDO). The rate constant of RhB degradation by the NiCoFe-LDO ($k = 0.269\ min^{-1}$) was 12.8, 2.23, and 1.62 times higher than those of the NiFe-LDO, NiCo-LDO, and CoFe-LDO, respectively (Fig. S7). The highest RhB decomposition efficiency of 97.86% by NiCoFe-LDO catalyst could be attributed to its optimum condition of high crystallinity and large surface area, which provide more active sites on the catalyst surface. Therefore, it can increase the PMS activation for forming more reactive oxygen species, thus increasing the RhB degradation. Hence, the NiCoFe-LDO catalyst was chosen for subsequent studies.

The UV-Vis absorption spectra of RhB solution during the reaction were also investigated in the range of 200-700 mm and the results are exhibited in Fig. S8. It can be observed that the RhB molecule has three characteristic peaks at wavelengths of 260 nm for benzene ring, 353 nm for naphthalene ring linking with –C=N– group, and 554 nm is the n-π* interaction of C = N and C = O groups [41]. The decreased intensity during the reaction time at peaks of 260 and 353 nm indicates the degradation of benzene and naphthalene rings of RhB. Meanwhile, the intensity of the peak at 554 nm was rapidly decreased during the reaction, which could be the N-de-ethylation of RhB and the loss of carboxyphenyl group, leading to the degradation of the color structure of RhB [42, 43].

The catalyst content directly affects the efficiency of RhB degradation due to the available number of Co(II), Ni(II), and Fe(III) active sites for the PMS activation. As seen in, The RhB removal efficiency after 14 min rapidly increased from 5% to 46.6% (Fig. 5(a)), and the rate constant increased 39.1 times (Fig. S9) when adding 20 mg/L of catalyst. With further increase of catalyst content to 60 mg/L, the efficiency rapidly increased to 97.86%. This can be attributed to the generation of more active sites with the increase of catalyst exposed to the environment, in which high catalyst content provides more transition metal ions as active sites for PMS activation to produce more radicals (e.g., $SO_4^{\bullet-}$, $OH^{\bullet}$, $O_2^{\bullet-}$, and $^1O_2$) for pollutant decomposition [22, 25, 26]. The catalyst contents from 60-120 mg/L provided similar removal efficiency (98.57-99.19%) and rate constant (0.2690-0.3574 min^{-1}) because the excess of metal ions such as Ni^{2+}, Co^{2+}, and Fe^{2+} could quench the produced radicals. Consequently, the catalyst content of 60 mg/L was chosen for the next investigations.

As depicted in Fig. 5(b), the RhB degradation efficiency after 14 min increased from 33 to 97.86% when PMS concentration increased from 100 to 500mg/L, where it reached the highest efficiency with a rate constant of 8.8 and 3.3 times higher than the PMS content of 100 and 300 mg/L, respectively (Fig. S10). The increase in PMS content creates favorable conditions for the generation of radicals by adsorbing more HSO_5^- on the catalyst surface. With further increases of PMS content to 750 and 1000 mg/L, the RhB treatment efficiency did not change significantly in the range of 97.86-98.58%. This is because the resulting sulfate radical can react with itself and be decomposed by residual PMS according to Reactions 1 and 2. Therefore, 500 mgPMS/L was selected for the subsequent experiments.

$$SO_4^{\bullet-} + SO_4^{\bullet-} \rightarrow S_2O_8^{2-} \quad \text{(Re. 1)}$$

$$HSO_5^- + SO_4^{\bullet-} \rightarrow SO_5^{\bullet-} + SO_4^{2-} + H^+ \quad \text{(Re. 2)}$$

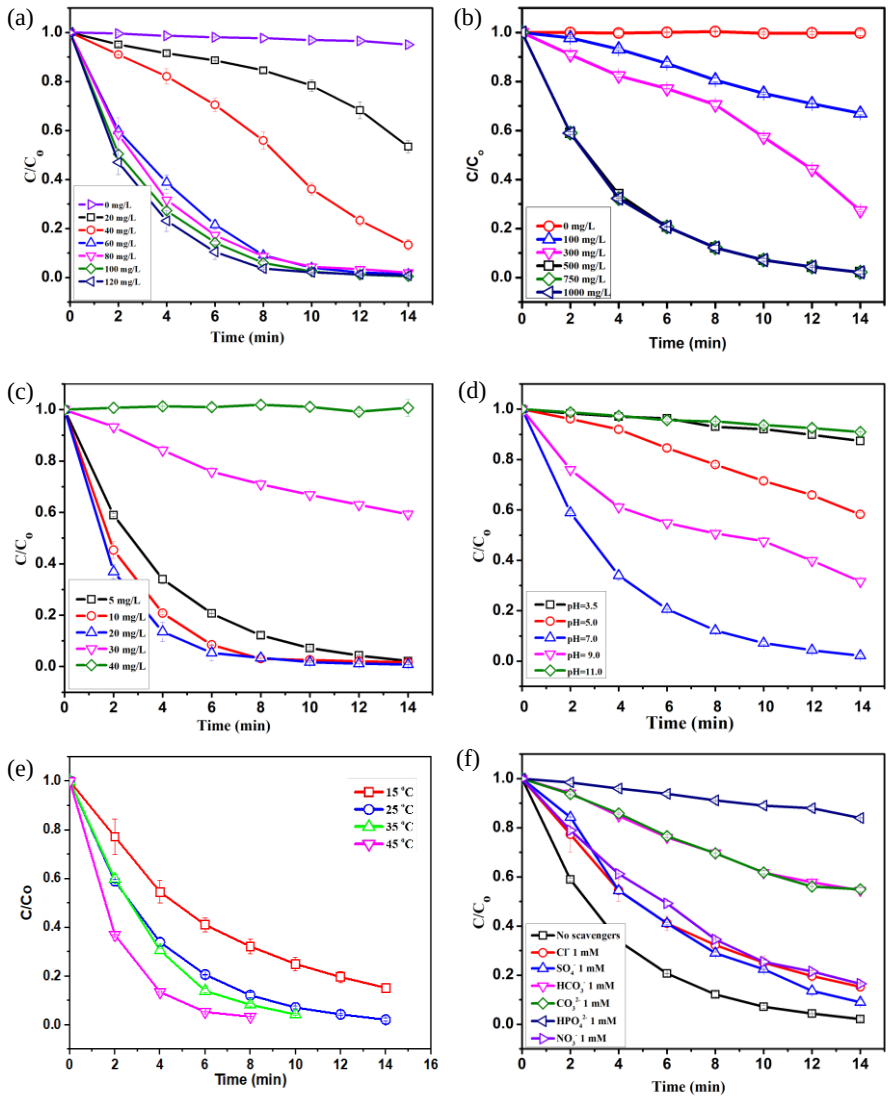

410

411 Fig. 5. Effects of (a) catalyst content, (b) PMS content, (c) RhB concentration, (d) solution pH,

412 (e) reaction temperature, and (f) anion on RhB removal

As observed in Fig. 5(c), an increase in RhB concentration reduced its decomposition efficiency and extended the treatment time to meet the target outlet concentration. RhB can be almost completely degraded at initial concentrations of 5-20 mg/L after 14 min of treatment with a rapid removal in the first 2 min and insignificant change after 6 min. The removal efficiency dropped to 41% at a concentration of 30 mg/L and was almost not removed during 14 min of treatment with the concentration of 40 mg/L. With the fixed condition of PH and content of catalyst and PMS, the production amount of reactive oxygen species is fixed, and it requires a longer time to remove RhB. Moreover, when RhB concentration is too high (e.g. 40 mg/L), it is adsorbed on the catalyst surface and occupied the position of active sites for PMS activation, thus reducing the formation of the active oxygen species for RhB degradation [25].

The pH value of the solution can affect the surface charge of the catalyst and the speciation of PMS and RhB, and therefore the formation of active oxygen species. PMS exists in the form of HSO_5^- in the pH range of 4-8 (pKa1 < 0 and pKa2 = 9.4). At pH = 9.4, PMS exists in HSO_5^- and SO_5^{2-} forms with about 50% for each form. When pH > 9.4, the existing form of PMS is SO_5^{2-} [44]. As demonstrated in Fig. S11, the pH_{pzc} of the catalyst surface was determined to be 7.7, which is the pH condition that the catalyst surface has no charge. When the solution pH is smaller pH_{pzc}, the catalyst surface has a positive charge and vice versa. As observed in Fig. 5(d), the pH 3.5 condition strongly inhibited the decomposition of RhB with low efficiency of 12.61% after 14 min of reaction. This is because the interaction between H^+ (under high proton concentration of low pH) and O-O in PMS reduces the adsorption of PMS on the surface of the material, leading to a decrease in PMS activation. Furthermore, H^+ ions can also react with active free radicals such as $SO_4^{\bullet-}$ and $OH^\bullet$ to form inactive forms of $HSO_4^\bullet$ and H_2O, respectively, according to Reactions 3 and 4.

436 $SO_4^{\bullet-} + H^+ + e^- \rightarrow HSO_4^{\bullet}$ (Re. 3)

437 $HO^{\bullet} + H^+ + e^- \rightarrow H_2O$ (Re. 4)

438 When pH increased from 5.0 to 7.0, the RhB treatment efficiency rapidly increased from 41.79%
439 to 97.86%. The rate constants of RhB degradation at pH = 7.0 (0.2690 min^{-1}) were 6.9 and 28.6
440 times higher than those at pH 5.0 and 3.5, respectively (Fig. S12). At pH = 7.0, PMS exists in the
441 form of HSO_5^- while the surface of the material has a positive charge, thus enhancing the
442 adsorption ability of HSO_5^- on the surface of the material. This increases the activation ability and
443 the degradability of RhB, which exists in a dielectric form ($RhB^{\pm}$). At pH 9 ($pH > pH_{pzc}$), there is
444 an electrostatic repulsion of the negatively charged surface with both the anionic form of RhB and
445 HSO_5^- and SO_5^{2-} forms of PMS, thereby reducing the possibility of activating PMS and the RhB
446 removal. Furthermore, in a strongly alkaline environment, the sulfate radical would convert to a
447 weaker radical ($HO^{\bullet}$), which reduces the ability to degrade RhB (Reaction 5). These are severely
448 observed at pH 11, where SO_5^{2-} is the main existing form of PMS is, with a very low removal
449 efficiency of only 9.08% after 14 min of reaction. Therefore, pH 7 was chosen for further
450 investigations.

451 $SO_4^{\bullet-} + HO^- \rightarrow HO^{\bullet} + SO_4^{2-}$ (Re. 5)

452 The effect of reaction temperature on the removal of RhB was investigated in the range of 15-45
453 ^oC (Fig. 5(e)), showing a promotion effect of reaction temperature. At a low temperature of 15 ^oC,
454 84.79% of RhB removal reached after 14 min of reaction, while at higher temperatures of 25, 35,
455 and 45 ^oC, 95% of RhB was removed after 14, 10, and 8 min, respectively. The reaction at different
456 temperatures also follows the pseudo-first-order kinetics ($R^2 \geq 0.9839$), where the rate constant
457 increases 3.24 times when reaction temperature increases from 15 to 45 ^oC (Table S2). This
458 enhancement is due to the faster production of sulfate radical by activating PMS at high

temperatures [45] and the improvement in the mass transfer of the pollutants and the radicals on the catalyst surface [46].

The relationship of temperature and reaction rate constant is described by the Arrhenius equation:

$$k = C/C_0 = Ae^{-\frac{Ea}{RT}} \quad \text{(Eq. 3)}$$

Hence, $$\ln k_{app} = \ln(C/C_0) = -\frac{Ea}{R}\frac{1}{T} + \ln A \quad \text{(Eq. 4)}$$

Where k_{app} is the rate constant of RhB degradation, Ea is the activation energy (kJ/mol), R is the ideal gas constant (8.314 J/(mol.K), T is the absolute temperature (K), and A is the frequency or pre-exponential factor (constant).

As presented in Fig. S13, the good linear relationship between $\ln k_{app}$ and 1/T with $R^2 = 0.973$ indicates the suitability of the Arrhenius equation. The activation energy (Ea) was determined to be 29.12 kJ/mol, which is higher than the Ea value (10-13 kJ/mol) of the reaction under diffusion control [47]. Thus, the apparent reaction rate constant in our work is determined by the surface reaction rate of RhB on NiCoFe-LDO material instead of the mass transfer rate. Moreover, the activation energy value in NiCoFe-LDO/PMS system is lower than those reported in the literature of 30.8 kJ/mol for MgCuFe-LDH/PMS [45], 56.9 kJ/mol for CoAl-LDO/PMS [22], 76.83 kJ/mol for CoMnAl-LDO/PMS [46], and 45,36 kJ/mol for $CoFe_2O_4$/ OSC/PMS [47].

Surface water, groundwater, and wastewater contain different anions which can absorb on the surface of the catalyst and react with reactive oxygen species (i.e., extinguishes the radicals), affecting the RhB degradation. The effect of anions Cl^-, SO_4^{2-}, NO_3^-, HCO_3^-, CO_3^{2-}, and HPO_4^{2-} using sodium salts on the RhB removal is illustrated in Fig. 5(f) and Fig. S14 at concentrations of 1 mM and 10 mM, respectively. The presence of NO_3^-, Cl^-, and SO_4^{2-} ions at a concentration of 1 mM caused a slight decrease in RhB degradation with efficiencies of 83.52, 84.8, and 91.01%,

481 respectively, but their concentration at 10 mM significantly inhibited the RhB degradation with
482 efficiencies of 77.56, 74.08, and 72.08%, respectively. At high salt concentrations, anions adsorb
483 onto the catalyst surface, thus reducing its ability to activate PMS. Among the anions, SO_4^{2-} has a
484 strong inhibiting effect at the concentration of 10 mM. On the other hand, since anions react with
485 radicals to form new radicals with weaker oxidizing potential, the degradation of RhB is reduced.
486 Specifically, Cl^- can react with sulfate and hydroxyl radicals to produce chlorine radicals of $Cl^{\bullet}$,
487 $Cl_2^{\bullet-}$, and $ClHO^{\bullet-}$ (E^o $Cl^{\bullet}/Cl^-$ = 2.4 V and E^o $Cl_2^{\bullet-}/2Cl^-$ = 2.1 V). These radicals are weaker
488 oxidizers than sulfate radicals (Eo $SO_4^{\bullet-}/SO_4^{2-}$ = 2.5 - 3.1V) through Reactions 6-11, which is also
489 reported in the literature [25].

490 $SO_4^{\bullet-} + NO_3^- \rightarrow SO_4^{2-} + NO_3^{\bullet}$ (Re. 6)

491 $SO_4^{\bullet-} + Cl^- \rightarrow SO_4^{2-} + Cl^{\bullet}$ (Re. 7)

492 $Cl^{\bullet} + Cl^- \rightarrow Cl_2^{\bullet-}$ (Re. 8)

493 $HO^{\bullet} + Cl^- \rightarrow ClHO^{\bullet-}$ (Re. 9)

494 $ClOH^{\bullet-} + H^+ \rightarrow Cl^{\bullet} + H_2O$ (Re. 10)

495 $2Cl^{\bullet} \rightarrow Cl_2$ (Re. 11)

496 On the other hand, HCO_3^-, CO_3^{2-} and HPO_4^{2-} anions strongly inhibit the decomposition of RhB,
497 which is more severe with the increase of anion concentration. At the concentration of 1 mM,
498 HPO_4^{2-} was the highest inhibitor for RhB degradation. The HPO_4^{2-} anion quenches sulfate radicals
499 to form less active phosphate radicals (Reaction 12). Moreover, the HPO_4^{2-} anion can form stable
500 complexes with Co^{2+} and Fe^{3+} ions on the catalyst surface, thus reducing PMS activation and
501 leading to a sharp decrease in RhB degradation efficiency. At a concentration of 10 mM, HCO_3^-,
502 CO_3^{2-}, and HPO_4^{2-}, the RhB degradation efficiency decreased significantly to 38.52, 3.94, and

16.1%, respectively. At this concentration, CO_3^{2-} anions almost completely inhibit RhB removal. The CO_3^{2-} and HCO_3^- anions can react or decompose $SO_4^{\bullet-}$ and $HO^{\bullet}$ according to Reactions 13-14 to form less active carbonate radicals. On the other hand, the presence of CO_3^{2-} makes the solution become highly alkaline, thus strongly inhibiting the decomposition of RhB due to the influence of solution pH as discussed above.

$$HPO_4^{2-} + SO_4^{\bullet-} \rightarrow HPO_4^{\bullet-} + SO_4^{2-} \quad \text{(Re. 12)}$$

$$HCO_3^- + SO_4^{\bullet-} \rightarrow HCO_3^{\bullet} + SO4^{2-} \quad \text{(Re. 13)}$$

$$HCO_3^- + HO^{\bullet} \rightarrow CO_3^{\bullet-} + H_2O \quad \text{(Re. 14)}$$

The durability of the NiCoFe-LDO is very important for its applications in practice, which was evaluated by the recycling test. After each test, the material was collected by using an external magnetic field, then washed with double-distilled water several times and ethanol for removing the organics on the surface, and finally dried at 70°C overnight before applying for the next test. The RhB removal efficiency was almost stable at 96.07-97.86% for the first 3 cycles, and then slightly decreased to 94.84% and 89.95% after 4 and 5 cycles, respectively (Fig. S15), proving the relatively high stability of the NiCoFe-LDO material. The decrease of RhB removal at 4^{th} and 5^{th} cycles can be attributed to the leaching of Ni, Co, and Fe metal ions that can lead to loss of active sites the contamination of the surfaces by adsorption of RhB degradation products [23]. The stability of the crystal structure of NiCoFe-LDO was determined through XRD analysis. The results in Fig. S16 show that is no obvious change in the diffraction peaks of NiCoFe-LDO after five cycles of reuse compared with the freshly prepared NiCoFe-LDO catalyst. However, a slight decrease in intensity at 36.72° peak of Co_3O_4 and 62.74° of Fe_3O_4 was observed, while the diffraction intensity slightly increased at 38.56° and 65.08° of Co_3O_4 before and after catalysis. It indicates the good stability of the crystalline structures of NiCoFe-LDO in the PMS catalyst

system. Ngoài ra, đường cong từ hóa của xúc tác NiCoFe-LDO sau 5 chu kỳ tái sử dụng được xác định, kết quả hình S4 cho thấy giá trị từ hóa bão hòa sau 5 chu kỳ sử là 27.20 emu/g cho thấy xúc tác NiCoFe-LDO vẫn được thu hồi tốt nhờ tính chất từ tính của nó. Cường độ từ hóa giảm nhẹ có thể do các sản phẩm phân hủy trung gian của RhB hấp phụ lên bề mặt của xúc tác [http://dx.doi.org/10.3390/catal10020225], đồng thời kết quả phân tích XRD cho thấy có sự giảm cường độ nhiễu xạ của Fe_3O_4 giảm đã ảnh hưởng đến cường độ từ hóa. The loss of Ni, Co, and Fe after the reaction was not significant through the ICP-MS analysis. The results show that at pH 3.0 after 14 minutes of reaction, the Ni, Co, and Fe contents in the solution were 0.07, 0.11, and 0.39 mg/L, respectively. At pH 7.0, the leached concentrations of these metals were 0.06, 0.06, and 0.17 mg/L, respectively. The leaching of Ni, Co, and Fe in the NiCoFe-LDO/PMS system is lower than the National standard for surface water QCVN 08-MT:2015/BTNMT of 0.1 mg/L and 0.5 mg/L (Column A1) for Ni and Fe, respectively, which indicates the stability of the NiCoFe-LDO catalyst.

3.3. Reaction mechanism

3.3.1. Determination of reactive oxygen radicals

The decomposition of RhB by the NiCoFe-LDO and PMS is described according to the formation and decomposition activities of active oxygen types such as superoxide ($O_2^{\bullet-}$), single oxygen $^1O_2$, sulfate radical ($SO_4^{\bullet-}$), hydroxyl radical ($HO^{\bullet}$), and peroxymonosulfate radical ($SO_5^{\bullet-}$). Among these radicals, $SO_5^{\bullet-}$ plays a minor role in RhB decomposition because of its weak oxidizing properties (E = 1.05V). Để xác định loại oxy hoạt động hình thành và quyết định sự phân hủy RhB bởi hệ NiCoFe-LDO/PMS, các thí nghiệm dập tắt triệt để được thực hiện bằng cách sử dụng các chất dập tắt chọn lọc TBA, IPA, EtOH, Phenol, FFA và p-BQ. Trong đó, TBA được dùng để dập tắt nhóm $^{\bullet}OH$ vì tốc độ phản ứng của TBA với $HO^{\bullet}$ nhanh hơn so với $SO_4^{\bullet-}$ khoảng 1000 lần

($k_{HO•}$ =3.8-7.6×10^8 $M^{-1}.s^{-}1$, $k_{SO4•-}$ = 4-9.1×10^5 $M^{-1}.s^{-1}$) [https://doi.org/10.1016/j.chemosphere.2020.128627]. Trong khi đó EtOH được xem là dập tắt cả $SO_4^{•-}$ và •OH bởi EtOH tốc độ phản ứng với nhóm HO• nhanh hơn gốc $SO_4^{•-}$ từ 36-75 lần ($k_{SO4•-}$ = 1.6-7.7×10^7 $M^{-1}.s^{-1}$; $k_{HO•}$ = 1.2-2.8×10^9 $M^{-1}.s^{-1}$)[49]. Ngoài ra, IPA phản ứng mạnh với cả HO• và $SO_4^{•-}$ với hằng số tốc độ phản ứng là 8.2×10^7 $M^{-1}.s^{-1}$ và 1.9×10^9 $M^{-1}.s^{-1}$ tương ứng [https://doi.org/10.1016/j.seppur.2020.117023]. Fufuryl ancohol (FFA) được sử dụng để dập tắt $^1O_2$ và •OH (k_{FFA-^1O2} = 1.2×10^8 $M^{-1}s^{-1}$; $k_{FFA-HO•}$ =1,5.10^{10} $M^{-1}s^{-1}$). Phenol được sử dụng để xác nhận sự hình thành của oxy đơn (k_{PheOH-^1O2} = 10^8 $M^{-1}s^{-1}$) [https://doi.org/10.1039/C8CP04852E, https://doi.org/10.1016/0045-6535(87)90004-X]. Ngoài ra, p-benzoquinone (p-BQ) được sử dụng để dập tắt hiệu quả $O_2^{•-}$ ($k_{O2•-}$ =0.9-1×10^9 $M^{-1}.s^{-1}$) [https://doi.org/10.1016/j.cej.2019.123361]. As presented in Fig. S17, the decomposition efficiency of RhB gradually decreased when adding quenching agents in the order of TBA (71.78%) ≈ IPA (68.98%) > EtOH (57.06%) > PheOH (31.71%) > FFA (27.12%) > p-BQ (8.64%). Kết quả cho thấy sử dụng FFA và PheOH để dập tắt $^1O_2$ cho kết quả tương đồng, điều đó cho thấy oxy đơn là một trong các loại oxy hoạt động chính hình thành trong hệ NiCoFe-LDO/PMS. Hơn nữa, để chứng minh vai trò của oxy hòa tan trong phân hủy RhB, Nito bão hòa được sục liên tục vào hệ phản ứng trước khi thêm PMS. Kết quả hình 17 a cho thấy khi oxy bị loại bỏ, hiệu quả phân hủy của Rhodamin B giảm mạnh còn 30,69%, điều đó cho thấy oxy hòa tan là cần thiết để tạo ta $O_2^{•-}$ và $^1O_2$ trong hệ NiCoFe-LDO/PMS, kết quả này cũng phù hợp với thí nghiệm dập tắt, trong đó $O_2^{•-}$ và $^1O_2$ đóng vai trò quyết định, kết quả này cũng được chỉ ra trong nghiên cứu của Chencheng Dong và cộng sự [https://doi.org/10.1016/j.apcatb.2021.120223]. The rate constant of RhB degradation in the absence of quenching agents (0.269 min^{-1}) was 3 and 40 times higher than those in the presence of TBA and p-BQ, respectively (Fig. S17). Thus, the order of radicals playing a role in RhB

degradation is $O_2^{\bullet-}$ > $^1O_2$ > $SO_4^{\bullet-}$ > $HO^{\bullet}$, in which the $O_2^{\bullet-}$ and $^1O_2$ radicals play a major role in RhB degradation, trong khi sự phân huỷ RhB bởi các gốc $SO_4^{\bullet-}$ và $HO^{\bullet}$ chiếm ở một mức độ nhỏ hơn nhiều.

Hơn nữa, các loại oxy hoạt động được xác nhận bằng phân tích EPR. Ở đây, DMPO được sử dụng làm chất bẫy spin cho $SO_4^{\bullet-}$, $HO^{\bullet}$ và $O_2^{\bullet-}$ trên cơ sở tín hiệu của DMPO-X (X: SO_4, OH và OOH) [https://doi.org/10.1016/j.cej.2019.123361], trong khi TEMP được sử dụng cho $^1O_2$ trên cơ sở tín hiệu TEMP-O [https://doi.org/10.1016/j.jhazmat.2019.121350] (Hình. Sơ đồ…) kết quả được đưa ra ở hình…..

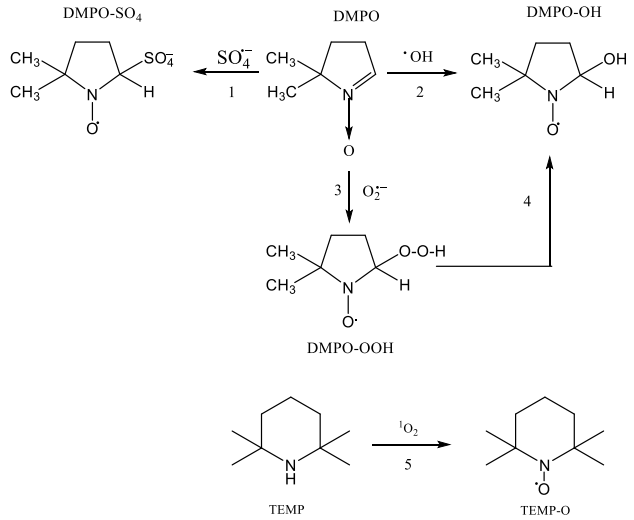

Hình. Sơ đồ phản ứng giữa DMPO và TEMP với các loại oxy hoạt động

Kết quả cho thấy, không có tín hiệu DMPO-X và TEM-O nào được quan sát trong hệ thống PMS một mình. Tuy nhiên, khi có mặt xúc tác NiCoFe-LDO, không quan sát thấy bất kỳ tín hiệu nào của DMPO-OH và DMPO-SO_4 (không thể hiện dữ liệu ở đây) điều này có thể do nồng độ gốc

hydroxyl và sunphat thấp, đồng thời DMPO-SO_4 với thời gian tồn tại ngắn và độ nhạy thấp nên không quan sát thấy tín hiệu [https://doi.org/10.1016/j.cej.2020.125903].

Hơn nữa, để nhận diện $O_2^{\bullet-}$, người ta sử dụng etanol làm dung môi (thay vì nước) để dập tắt $SO_4^{\bullet-}$ và $HO^{\bullet}$, ngăn chặn sự hình thành DMPO-OH hoặc DMPO-SO_4 [https://doi.org/10.1016/j.chemosphere.2018.11.197]. Như quan sát trong hình …a, có thể quan sát thấy bốn đỉnh đặc trưng (1:1:1:1) có cường độ mạnh, cho thấy sự hiện diện của các gốc superoxide, kết quả EPR phù hợp với các thí nghiệm dập tắt, chỉ ra rằng $O_2^{\bullet-}$ chịu trách nhiệm chính cho sự suy thoái của RhB. Hơn nữa, khi thêm p-BQ cường độ các đỉnh đặc trưng của DMPO-OOH của giảm rõ rệt, điều đó cho thấy một lượng lớn $O_2^{\bullet-}$ được hình thành trong hệ NiCoFe-LDO/PMS. Mặt khác, oxy đơn được nhận diện trên cơ sở tín hiệu TEMP-O, kết quả EPR hiển thị tín hiệu của ba đường có cường độ bằng nhau (1: 1: 1) của các sản phẩm TEMP-O, chứng tỏ sự có mặt của $^1O_2$. Do đó, nó chỉ ra rằng còn đường phi truyền thống tạo thành không gốc xảy ra trong quá trình hoạt hóa PMS bởi NiCoFe-LDO. Hơn nữa, khi có mặt p-BQ, cường độ tín hiệu TEMP-O giảm mạnh, điều đó cho thấy các gốc superoxide trong trường hợp này đã tham gia vào việc chuyển đổi thành $^1O_2$ [https://doi.org/10.1016/j.apcatb.2021.120223]. Do đó, kết quả EPR cũng xác nhận $O_2^{\bullet-}$ và $^1O_2$ là các loài phản ứng chính gây ra sự phân ủy RhB trong khi $SO_4^{\bullet-}$ và $HO^{\bullet}$ đóng vai trò hạn chế. Kết quả này cũng được chỉ ra trong một số hệ Fe_3O_4@C/PB/PMS/ 2,4-DCP [https://doi.org/10.1016/j.chemosphere.2018.11.197], $MoSe_2$/PMS/Vis [https://doi.org/10.1016/j.apcatb.2021.120223], Fe^0-montmorillonit/PMS [https://doi.org/10.1016/j.cej.2018.04.175]. Như vậy, sự kết hợp các thí nghiệm dập tắt và phân tích EPR chỉ ra rằng $O_2^{\bullet-}$ và $^1O_2$ được hình thành chính trong hệ NiCoFe-LDO/PMS, theo hiểu biết của chúng tôi đây là công bố đầu tiên về xúc tác LDO có thể hoạt hóa hiệu quả PMS hình

thành chủ yếu $O_2^{\bullet -}$ và $^1O_2$, khác với hầu hết các LDO khác hoạt hóa PMS (bảng S3) tạo ra $SO_4^{\bullet -}$ và $HO^{\bullet}$. loại bỏ các chất ô nhiễm hữu cơ trong nước.

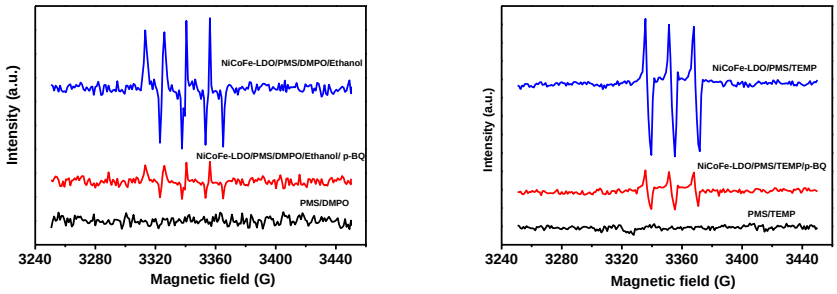

Hình. (a) EPR spectra for the detection of $O_2^{\bullet -}$ in the presence of DMPO and ethanol at room temperature; (b) EPR spectra for the detection of $^1O_2$ in the presence of TEMP at room temperature (Experimental conditions: 1.2 mmol/L PMS, 0.3 g/L MoSe2, light source: 300 W Xe lamp with 420 nm cut filter).

(*Condition: [NiCoFe-LDO]=60 mg/L, [PMS]=500mg/L, [DMPO]=40mM, [TEMP]=20mM, [p-BQ]=1mM, pH 7.0, 25 °C*)

3.3.2. Degradation pathway of RhB by NiCoFe-LDO/PMS system

The degradation of RhB by NiCoFe-LDO/PMS to intermediate products was determined by MS. The structure of RhB contains nitrogen atoms, thus it is suitable for the positive ion ionization (ESI+) technique [48]. The degradation of RhB by ROS mainly occurs through 4 main processes: N-de-ethylation, cleavage of color-bearing group, xanthene ring-opening, and mineralization [49, 50], as proposed in Fig. 6. Rhodamine B was identified by m/z = 443 [51]. In the first stage, the de-ethylation in the RhB structure forms M1 (m/z = 415) [51] and the N-de-ethylation forms M2 (m/z=374). On the other hand, ROS break the C-Phenyl bond to remove the benzoic acid from the xanthene ring, forming M3 (m/z = 322). The decarboxylation and hydroxylation of M2 form M4

(m/z = 307). The cleavage of the C-Phenyl bond, removal of the ethyl group, and the hydroxylation of M1 and M3 produce M5 (m/z = 285). After that, M6 (m/z = 232) was formed from several processes such as C-Phenyl bond cleavage, N-de-ethylation, and hydroxylation of M4 and M5, leading to the decolorization of RhB [52]. The products from M2-M6 were only found in this study, but not found by other works. The dehydroxylation of M6 then forms M7 (m/z = 197) and M8 (m/z = 181) by removing 2 and 3 hydroxyl groups, respectively [53]. In the second stage, ROS directly react with xanthene and open the ring to form M9 (phthalic acid, m/z = 166) [54], open-chain organic acids such as M10 (3-hexenedioic acid, m/z = 144), M11 (propanoic acid, m/z = 74) and M12 (acetic acid, m/z = 60) [51, 55]. Finally, the mineralization of these open-chain organic acids forms the final products of CO_2, H_2O, NO_3^-, and NH_4^+.

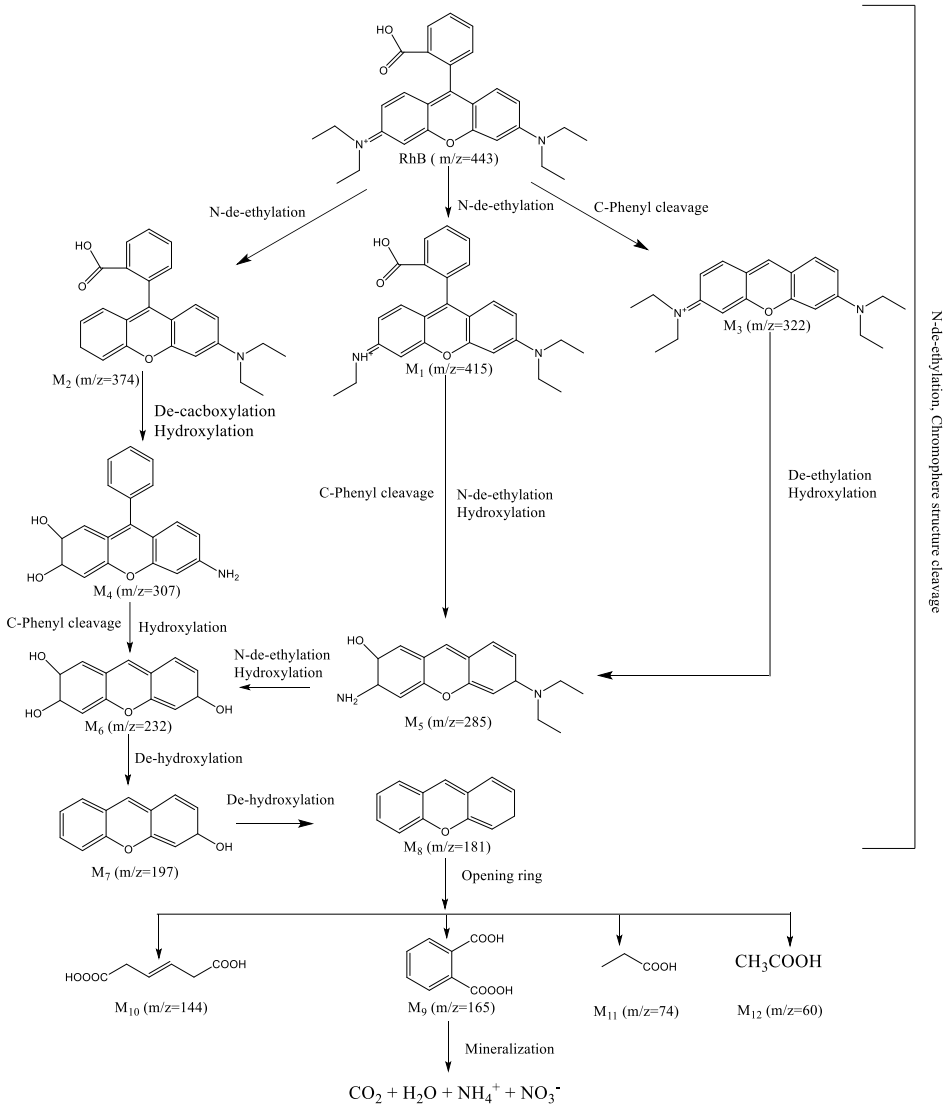

Fig. 6. The possible degradation pathway of RhB in the NiCoFe-LDO/PMS system.

Để đánh giá khả năng khoáng hóa của RhB bởi hệ NiCoFe-LDO/PMS, COD của dung dịch phản ứng được xác định và kết quả được mô tả trong hình ….. Việc loại bỏ COD đạt được 32.25; 74.87 và 98.33 sau 7; 14 và 30 phút phản ứng. Sự khoáng hóa của RhB là tương đối cao so với một số

hệ α-MnO_2/PMS là 61 % sau 30 phút phản ứng [https://doi.org/10.1007/s11270-016-2782-6], CoMn/SBA-15/PMS là 45% sau 30 phút [https://doi.org/10.1016/j.seppur.2021.119081]

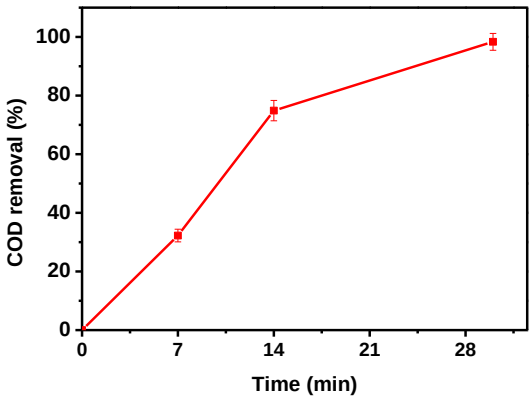

Hình. Hiệu quả loại bỏ COD của RhB theo thời gian bởi hệ NiCoFe-LDO/PMS

3.3.4. Proposing the reaction mechanism

Trên cơ sở kết quả phân tích XPS, nhận diện loại oxy hoạt động ở trên, cơ chế suy thoái RhB trong hệ NiCoFe-LDO/PMS bao gồm hai quá trình oxy hóa gốc và không gốc.The PMS activation mechanism by NiCoFe-LDO for the decomposition of RhB is proposed in Fig. 7. After adding PMS, Co^{2+}, Fe^{2+}, and Ni^{2+} ions on the catalyst surface can activate HSO_5^- to form $SO_4^{\bullet-}$, and Co^{3+}, Fe^{3+}, and Ni^{3+} (Reactions 15. Then, Co^{3+}, Fe^{3+}, and Ni^{3+} can be reduced to Co^{2+}, Fe^{2+}, Ni^{2+} by reacting with HSO_5^- and produce a weak oxidizing $SO_5^{\bullet-}$ radical (Reactions 16) [https://doi.org/10.1016/j.seppur.2020.117685]. Besides, there are also interactions between metal ions (Reactions 17-19). Trong hệ NiCoFe-LDO/PMS, sự hiện diện của $O_2^{\bullet-}$ có thể được giải thích từ các quá trình sau: (i) Các chỗ trống oxy (oxygen vacancies-OVs) trên bề mặt của LDO giàu electron sẽ hoạt hóa oxy hòa tan hình thành $O_2^{\bullet-}$ (phản ứng 20) trên bề mặt pha rắn (vai trò của oxy hòa tan đã được chỉ ra ở mục 3.3.1), tham gia hiệu quả vào quá trình phản ứng với chất ô nhiễm [https://doi.org/10.1016/j.cej.2018.04.215]. (ii) Phản ứng phân ly HSO_5^- thành SO_5^{2-} (phản ứng 21), quá trình phản ứng của SO_5^{2-}, HSO_5^- với nước tạo thành H_2O_2 và SO_4^{2-} (phản ứng 22). Sự khử các ion kim loại hóa trị ba bởi H_2O_2 tạo thành $O_2^{\bullet-}$ (phản ứng 23), phản ứng tái tạo kim loại hóa trị hai bởi $O_2^{\bullet-}$ (phản ứng 24) để hoạt hóa PMS mang lại hiệu quả cao cho quá trình phân

hủy RhB [https://doi.org/10.1016/j.seppur.2020.117685].(iii) The sulfate radical is partially converted to hydroxyl radical in the presence of H_2O (Reactions 25), sự chuyển hóa gốc sunphat thành gốc hydroxyl có thể đã làm giảm nồng độ của nó trong dung dịch và không phát hiện được tín hiệu EPR, phản ứng phân hủy gốc hydoxyl bởi hydropeoxit (phản ứng 26), hình thành gốc hydroperoxyl, sau đó phân ly thành gốc supeoxit (phản ứng 27) [https://doi.org/10.1016/j.apcatb.2021.120223]. Sự phân hủy các gốc hydroxyl có thể dẫn tới làm giảm mạnh nồng độ của nó, dẫn đến không phát hiện tín hiệu EPR của DMPO-OH. Cơ chế thứ hai chiếm ưu thế trong hệ NiCoFe-LDO/PMS là quá trình oxi hóa phi truyền thống với sự hình thành của oxy đơn $^1O_2$ được xác nhận từ thí nghiệm dập tắt và EPR. Một số phản ứng có liên quan đến sự hình thành $^1O_2$ từ phản ứng giữa HSO_5^- và SO_5^{2-} (phản ứng 28), phản ứng phân hủy gốc peroxymonosulfate ($SO_5^{\bullet-}$) bởi nước (phản ứng 29) [https://doi.org/10.1016/j.chemosphere.2018.11.197], chuyển hóa gốc superoxit và hydroxyl (phản ứng 30) [https://doi.org/10.1016/j.cej.2020.127066][https://doi.org/10.1016/j.seppur.2021.118666]. Ngoài ra, oxy đơn còn được hình thành từ phản ứng của các loại oxy hấp phụ (O_{ads}) (phản ứng 31-32) [https://doi.org/10.1016/j.seppur.2021.118666], điều này được xác nhận bởi sự thay đổi của O_{ads} trước và sau xúc tác. Active oxygen species produce $O_2^{\bullet-}$, singlet oxygen ($^1O_2$), sulfate radical ($SO_4^{\bullet-}$), and hydroxyl radical ($HO^{\bullet}$) participate in the oxidation of RhB to form intermediate molecules and further inorganic substances (Reactions 33-34).

$$\equiv M^{2+} + HSO_5^- \rightarrow \equiv M^{3+} + SO_4^{\bullet-} + OH^- \quad \text{(Re. 15)}$$

$$\equiv M^{3+} + HSO_5^- \rightarrow \equiv M^{2+} + SO_5^{\bullet-} + H^+ \quad \text{(Re. 16)}$$

$$\equiv Ni^{3+} + \equiv Co^{2+} \rightarrow \equiv Co^{3+} + \equiv Ni^{2+} \quad \text{(Re. 17)}$$

$$\equiv Fe^{3+} + \equiv Co^{2+} \rightarrow \equiv Co^{3+} + \equiv Fe^{2+} \quad \text{(Re. 18)}$$

$$\equiv Fe^{3+} + \equiv Ni^{2+} \rightarrow \equiv Ni^{3+} + \equiv Fe^{2+} \quad \text{(Re. 19)}$$

$$O_2 + e^- \rightarrow O_2^{\bullet-} \quad \text{(Re. 20)}$$

$$HSO_5^- \rightarrow SO_5^{2-} + H^+ \quad \text{(Re. 21)}$$

HSO_5^- (SO_5^{2-}) + H_2O → H_2O_2 + HSO_4^- (SO_4^-) (Re. 22)

$\equiv M^{3+} + H_2O_2 \rightarrow \equiv M^{2+} + O_2^{\bullet-} + 2H^+$ (Re. 23)

$\equiv M^{3+} + O_2^{\bullet-} \rightarrow \equiv M^{2+} + O_2$ (Re. 24)

$SO_4^{\bullet-} + H_2O \rightarrow HO^{\bullet} + HO^-$ (Re. 25)

$HO^{\bullet} + H_2O_2 \rightarrow HO_2^{\bullet} + H_2O$ (Re. 26)

$HO_2^{\bullet} \rightarrow O_2^{\bullet-} + H^+$ (Re. 27)

$SO_5^{2-} + HSO_5^- \rightarrow {}^1O_2 + 2SO_4^- + H^+$ (Re. 28)

$2SO_5^{\bullet-} + H_2O \rightarrow 1.5\ {}^1O_2 + 2HSO_4^-$ (Re. 29)

$O_2^{\bullet-} + HO^{\bullet} \rightarrow {}^1O_2 + HO^-$ (Re. 30)

$O_{ads} \rightarrow O^*$ (Re. 31)

$O^* + HSO_5^- \rightarrow {}^1O_2 + HSO_4^-$ (Re. 32)

$O_2^{\bullet-} + {}^1O_2 + SO_4^{\bullet-} + HO^{\bullet}$ + RhB → intermediates + SO_4^{2-} (Re. 33)

$O_2^{\bullet-} + {}^1O_2 + SO_4^{\bullet-} + HO^{\bullet}$ + intermediates → $H_2O + CO_2 + SO_4^{2-}$ (Re. 34)

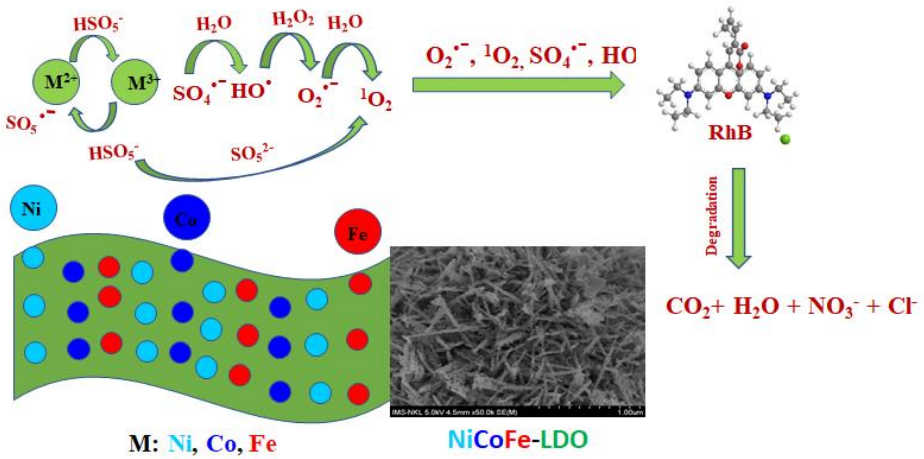

Fig. 7. Proposed mechanism for degradation of RhB in water using NiCoFe-LDO material for PMS activation

3.3. Treatment of other dyes and in different water environments

The PMS activation by NiCoFe-LDO was applied for treating various textile dyes, including xanthene group (RhB), azo (TTZ, OG, JGB, DB71, and MO), and phenothiazine (MB). Fig. 8(a) shows that the degradation efficiency after 14 min of the dyes was in the order of RhB (97.86%) > OG (70.55%) > DB71 (56.98%) ≈ MO (56.0%) ≈ TTZ (55.83%) ≈ JGB (55.22%) ≈ MB(53.56%). Sau 30-40 phút, trên 95% các thuốc nhuộm còn lại đều bị phân hủy (dữ liệu không được hiển thị ở đây), một số hệ cần thời gian loại bỏ các thuốc nhuộm dài hơn như NiO-$NiFe_2O_4$-rGO/PMS sau 40 phút loại bỏ hoàn toàn RhB [doi:10.3390/w11020384], $CoFe_2O_4$/ZIF-8/PMS sau 60 phút phân hủy 97.9% MB [https://doi.org/10.1016/j.chemosphere.2019.125021], Fe_3O_4@ C/Co/PMS loại bỏ AO7 hoàn toàn sau 40 phút [DOI: 10.1039/C5RA13078F], $MnFe_2O_4$/rGO/PMS loại bỏ hoàn toàn methyl dacam sau 40 phút, metyl xanh sau 120 phút, rhodamin B, dacam II sau 240-270 phút [http://dx.doi.org/doi:10.1016/j.jhazmat.2014.01.027]. Different molecular structures of the dyes

resulted in different selectivity of the radicals formed during the PMS activation by NiCoFe-LDO material. The degradation kinetics of OG, TTZ, JGB, and MB followed pseudo-first-order kinetics with $R^2 \geq 0.943$ while those of DB71 and MO did not, which could be due to their complex molecular structures that require multi-step reactions during the decomposition process (Fig. S18).

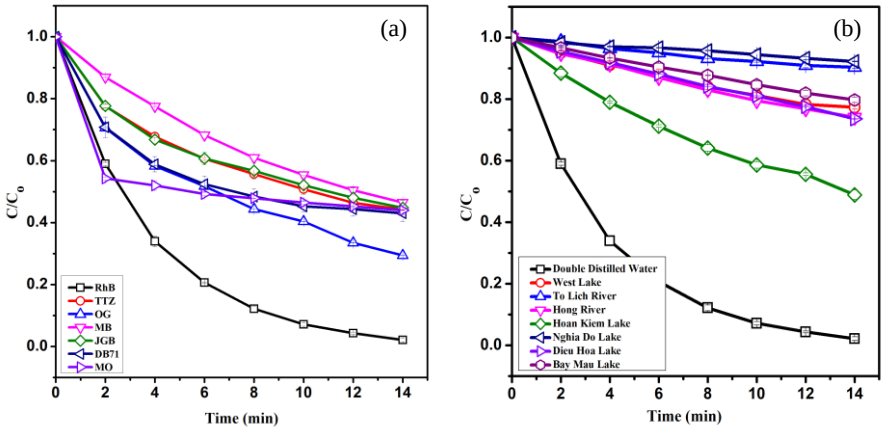

Fig. 8. Ability of NiCoFe-LDO and PMS to decompose (a) different dyes in water and (b) RhB dye in different types of natural surface water

(*Condition: 20 mgdye/L, 500 mgPMS/L, 60 mgLDO/L, pH 7.0, 25 °C*)

This study also evaluated the treatment of RhB in water taken from many rivers (To Lich and Hong) and lakes (West, Hoan Kiem, Bay Mau, Dieu Hoa, and Nghia Do) in Hanoi (Vietnam). As shown in Fig. 8(b), the RhB degradation after 14 min reached 97.86% in double distilled water but was strongly inhibited in the water of Hoan Kiem Lake (51.1%) > Dieu Hoa Lake (26.43%) ≈ Hong River (25.92%) > West Lake (22.68%) > Bay Mau Lake (20.28%) > To Lich River (9.65%) > Nghia Do Lake (7.73%). The rate constants of RhB degradation in double distilled water was 2

and 49 times higher than those in the water of Hoan Kiem Lake and Nghia Do Lake, respectively (Fig. S19). Kết quả xác định một số thông số cơ bản trong nước mặt sông, hồ được đưa ra ở bảng… hàm lượng các thông số ô nhiễm như COD, clorua, amoni và photphat đều vượt tiêu chuẩn cho phép của QCVN 08:2015 (Column A2) của nước mặt. Cụ thể, hàm lượng COD vượt quá tiêu chuẩn cho phép từ 1.15-3.41 lần, hàm lượng clorua, photphat, amoni cao hơn từ 2.23-15.22; 2-31, 4.5-56.4 lần tương ứng. Như vậy, so với nước cất hai lần, hiệu quả loại bỏ RB trong nước mặt bị ức chế mạnh. Điều này có thể là do sự tồn tại của các chất cạnh tranh như hàm lượng các chất ô nhiễm hữu cơ cao COD cao, đồng thời sự có mặt hàm lượng lớn anion clorua có thể gây ức chế do sự tạo thành các dạng clo hoạt động có tính oxi hóa yếu hơn. The inhibition of RhB degradation can be explained by the presence of high levels of ammonium and surfactants from domestic wastewater discharged directly into the lake, and high concentrations of dissolved organic substances. The natural colloidal particles with particle size from 1 nm - 1 µm could also adsorb on the catalyst surface, thus preventing the contact of the NiCoFe-LDO catalyst with PMS and greatly reducing the decomposition of RhB. Do đó, hiệu quả suy thoái RhB trong hệ thống NiCoFe-LDO/ PMS bị hạn chế trong các nền nước mặt khác.

Bảng: Các thông số cơ bản của nước sông hồ

Actual water samples	pH	COD (mg/L)	Cl^- (mg/L)	NO_3^- (mg/L)	PO_4^{3-} (mg/L)	NH_4^+ (mg/L)	TSS (mg/L)	Độ cứng $CaCO_3$ mg/L
West Lake	7.164	17.6	3550	0.82	0.41	2.52	3.2	310
To Lich River	7.334	51.2	2414	3.26	4.15	16.91	21.5	310
Hong River	6.881	17.8	781	1.13	0.68	1.94	13.2	120
Hoan Kiem lake	6.855	28.3	1633	0.92	3.58	1.51	54.4	210
Nghia Do Lake	6.509	48.6	5325	3.25	6.11	10.2	16.8	490
Dieu Hoa Lake	7.125	17.2	2873	1.25	0.47	1.36	13.5	270
Bay Mau Lake	6.543	43.4	4854	3.58	5.13	12.35	18.4	320
QCVN 08:2015 (Column A_2)	6-8.5	15	350	5	0.2	0.3	30	-

The application of NiCoFe-LDO 500/PMS in practical wastewater treatment was tested with real recalcitrant wastewater such as textile wastewater containing dyes (from Hopex Company, Hai Duong Province, Vietnam), redwater containing trinitrotoluene (from Hoa Phat Company, Quang Ninh Province, Vietnam), paper wastewater (from An Hoa Company, Tuyen Quang) and landfill leachate (from Nam Son landfill, Ha Noi) . The COD values of these wastewaters were 520, 450, 584, and 448 mg/L, which exceed the limit of 150 mg/L for discharging into the environment (QCVN 40:2011/BTNMT, Column B, National Technical Regulation on Industrial Wastewater). After being treated with NiCoFe-LDO 500/PMS system (500 mgPMS/L, 60 mgLDO/L, pH 7.0, 25 °C) for 60 min, the COD removal efficiency reached 62.23% for textile wastewater, 42.31% for redwater, 66.10% for paper wastewater and 71.43% for landfill leachate (Fig. S20). This implies that the PMS activation by NiCoFe-LDO could be a promising technology for the treatment of recalcitrant compounds in industrial wastewater.

The comparison of using different LDO catalysts for PMS or PS activation to remove the organics of this study and other works in the literature [22-27, 56, 57] is summarized in Table S3. It is difficult to compare the performance of different reaction systems since they used different LDO materials with diverse crystal phases and the reactions were conducted under various conditions. However, it can be seen that the NiCoFe-LDO material has the advantages of low contents of catalyst and PMS used for high organic concentration, fast decomposition, and high RhB removal efficiency. Besides, $O_2^{\bullet-}$, $^1O_2$, $SO_4^{\bullet-}$, and $HO^{\bullet}$ radicals play an important role in the RhB removal.

4. Conclusions

This study successfully synthesized NiCoFe-LDO material for PMS activation and applied it for removing RhB and some other dyes in water. The NiCoFe-LDO prepared at 500 ^oC had the highest

RhB removal efficiency of 97.86% after 14 min of reaction. This is due to the high surface area and crystallinity of the material at this temperature. The optimum condition was found to be 20 mg/L of RhB, 500 mg/L of PMS, 60 mg/L of NiCoFe-LDO, and pH 7.0. Via radical scavenging tests, the reactive oxygen species such as $O_2^{\bullet-}$, $^1O_2$, $SO_4^{\bullet-}$, and $HO^{\bullet}$ were determined to be the key radicals for the degradation of RhB. The reaction mechanism was also proposed to describe the activation of PMS by NiCoFe-LDO material and reaction pathways for decomposing RhB in water. The tests with various actual surface waters and wastewaters showed that PMS activation by NiCoFe-LDO material could be a promising technology for removing hard-biodegradable organic pollutants in practical applications.

References

[1] C. Huang, Y. Wang, M. Gong, W. Wang, Y. Mu, Z.-H. Hu, α-MnO_2/Palygorskite composite as an effective catalyst for heterogeneous activation of peroxymonosulfate (PMS) for the degradation of Rhodamine B, Sep. Purif. Technol., 230 (2020) 115877.

[2] T. Chankhanittha, S. Nanan, Visible-light-driven photocatalytic degradation of ofloxacin (OFL) antibiotic and Rhodamine B (RhB) dye by solvothermally grown ZnO/Bi2MoO6 heterojunction, J. Colloid Interface Sci., 582 (2021) 412-427.

[3] G. Chen, X. Zhang, Y. Gao, G. Zhu, Q. Cheng, X. Cheng, Novel magnetic MnO2/MnFe2O4 nanocomposite as a heterogeneous catalyst for activation of peroxymonosulfate (PMS) toward oxidation of organic pollutants, Sep. Purif. Technol., 213 (2019) 456-464.

[4] C.-Z. Liang, S.-P. Sun, B.-W. Zhao, T.-S. Chung, Integration of Nanofiltration Hollow Fiber Membranes with Coagulation–Flocculation to Treat Colored Wastewater from a Dyestuff Manufacturer: A Pilot-Scale Study, Ind. Eng. Chem. Res., 54 (2015) 11159-11166.

[5] W. Xiao, Z.N. Garba, S. Sun, I. Lawan, L. Wang, M. Lin, Z. Yuan, Preparation and evaluation of an effective activated carbon from white sugar for the adsorption of rhodamine B dye, J. Cleaner Prod., 253 (2020) 119989.

[6] T.A. Otitoju, D. Jiang, Y. Ouyang, M.A.M. Elamin, S. Li, Photocatalytic degradation of Rhodamine B using CaCu3Ti4O12 embedded polyethersulfone hollow fiber membrane, Journal of Industrial and Engineering Chemistry, 83 (2020) 145-152.
[7] T. Li, X. Du, J. Deng, K. Qi, J. Zhang, L. Gao, X. Yue, Efficient degradation of Rhodamine B by magnetically recoverable Fe3O4-modified ternary CoFeCu-layered double hydroxides via activating peroxymonosulfate, J. Environ. Sci., 108 (2021) 188-200.
[8] J. Hou, X. He, S. Zhang, J. Yu, M. Feng, X. Li, Recent advances in cobalt-activated sulfate radical-based advanced oxidation processes for water remediation: A review, Sci. Total Environ., 770 (2021) 145311.
[9] M. Kohantorabi, G. Moussavi, S. Giannakis, A review of the innovations in metal- and carbon-based catalysts explored for heterogeneous peroxymonosulfate (PMS) activation, with focus on radical vs. non-radical degradation pathways of organic contaminants, Chem. Eng. J., 411 (2021) 127957.
[10] J.R.J. Zaeni, J.-W. Lim, Z. Wang, D. Ding, Y.-S. Chua, S.-L. Ng, W.-D. Oh, In situ nitrogen functionalization of biochar via one-pot synthesis for catalytic peroxymonosulfate activation: Characteristics and performance studies, Sep. Purif. Technol., 241 (2020) 116702.
[11] Y. Ding, X. Wang, L. Fu, X. Peng, C. Pan, Q. Mao, C. Wang, J. Yan, Nonradicals induced degradation of organic pollutants by peroxydisulfate (PDS) and peroxymonosulfate (PMS): Recent advances and perspective, Sci. Total Environ., 765 (2021) 142794.
[12] U. Ushani, X. Lu, J. Wang, Z. Zhang, J. Dai, Y. Tan, S. Wang, W. Li, C. Niu, T. Cai, N. Wang, G. Zhen, Sulfate radicals-based advanced oxidation technology in various environmental remediation: A state-of-the–art review, Chem. Eng. J., 402 (2020) 126232.
[13] L. Jafari Foruzin, Z. Rezvani, Ultrasonication construction of the nano-petal NiCoFe-layered double hydroxide: An excellent water oxidation electrocatalyst, Ultrason. Sonochem., 64 (2020) 104919.
[14] G. Zhang, X. Zhang, Y. Meng, G. Pan, Z. Ni, S. Xia, Layered double hydroxides-based photocatalysts and visible-light driven photodegradation of organic pollutants: A review, Chem. Eng. J., 392 (2020) 123684.
[15] Z.-H. Xie, H.-Y. Zhou, C.-S. He, Z.-C. Pan, G. Yao, B. Lai, Synthesis, application and catalytic performance of layered double hydroxide based catalysts in advanced oxidation processes for wastewater decontamination: A review, Chem. Eng. J., 414 (2021) 128713.

[16] S. Mallakpour, M. Hatami, C.M. Hussain, Recent innovations in functionalized layered double hydroxides: Fabrication, characterization, and industrial applications, Adv. Colloid Interface Sci., 283 (2020) 102216.
[17] J. Deng, L. Xiao, S. Yuan, W. Wang, X. Zhan, Z.-H. Hu, Activation of peroxymonosulfate by CoFeNi layered double hydroxide/graphene oxide (LDH/GO) for the degradation of gatifloxacin, Sep. Purif. Technol., 255 (2021) 117685.
[18] K.A. Azalok, A.A. Oladipo, M. Gazi, UV-light-induced photocatalytic performance of reusable MnFe-LDO–biochar for tetracycline removal in water, J. Photochem. Photobiol. A, 405 (2021) 112976.
[19] S. Li, D. Wang, X. Wu, Y. Chen, Recent advance on VOCs oxidation over layered double hydroxides derived mixed metal oxides, Chin. J. Catal., 41 (2020) 550-560.
[20] L. Li, Q. Zhang, Y. She, Y. Yu, J. Hong, High-efficiency degradation of bisphenol A by heterogeneous Mn–Fe layered double oxides through peroxymonosulfate activation: Performance and synergetic mechanism, Sep. Purif. Technol., 270 (2021) 118770.
[21] H. Wu, Z. Zhao, G. Wu, Facile synthesis of FeCo layered double oxide/raspberry-like carbon microspheres with hierarchical structure for electromagnetic wave absorption, J. Colloid Interface Sci., 566 (2020) 21-32.
[22] J. Zhu, Z. Zhu, H. Zhang, H. Lu, Y. Qiu, Calcined CoAl-layered double hydroxide as a heterogeneous catalyst for the degradation of acetaminophen and rhodamine B: activity, stability, and mechanism, Environ Sci Pollut Res, 26 (2019) 33329-33340.
[23] Y. Hong, J. Peng, X. Zhao, Y. Yan, B. Lai, G. Yao, Efficient degradation of atrazine by CoMgAl layered double oxides catalyzed peroxymonosulfate: Optimization, degradation pathways and mechanism, Chem. Eng. J., 370 (2019) 354-363.
[24] L. Luo, Y. Wang, M. Zhu, X. Cheng, X. Zhang, X. Meng, X. Huang, H. Hao, Co–Cu–Al Layered Double Oxides as Heterogeneous Catalyst for Enhanced Degradation of Organic Pollutants in Wastewater by Activating Peroxymonosulfate: Performance and Synergistic Effect, Ind. Eng. Chem. Res., 58 (2019) 8699-8711.
[25] Y. Hong, H. Zhou, Z. Xiong, Y. Liu, G. Yao, B. Lai, Heterogeneous activation of peroxymonosulfate by CoMgFe-LDO for degradation of carbamazepine: Efficiency, mechanism and degradation pathways, Chem. Eng. J., 391 (2020) 123604.

[26] W. Li, P. Wu, S. Yang, Y. Zhu, C. Kang, L.T. Tran, B. Zeng, 3D hierarchical honeycomb structured MWCNTs coupled with CoMnAl–LDO: fabrication and application for ultrafast catalytic degradation of bisphenol A, RSC Adv., 5 (2015) 8859-8867.
[27] S. Zhou, C. Li, G. Zhao, L. Liu, J. Yu, X. Jiang, F. Jiao, Heterogeneous co-activation of peroxymonosulfate by CuCoFe calcined layered double hydroxides and ultraviolet irradiation for the efficient removal of p-nitrophenol, Journal of Materials Science: Materials in Electronics, 30 (2019) 19009-19019.
[28] X. Meng, M. Feng, H. Zhang, Z. Ma, C. Zhang, Solvothermal synthesis of cobalt/nickel layered double hydroxides for energy storage devices, J. Alloys Compd., 695 (2017) 3522-3529.
[29] Z. Lu, L. Qian, W. Xu, Y. Tian, M. Jiang, Y. Li, X. Sun, X. Duan, Dehydrated layered double hydroxides: Alcohothermal synthesis and oxygen evolution activity, Nano Research, 9 (2016) 3152-3161.
[30] S.-B. Lee, E.-H. Ko, J.Y. Park, J.-M. Oh, Mixed Metal Oxide by Calcination of Layered Double Hydroxide: Parameters Affecting Specific Surface Area, Nanomaterials, 11 (2021) 1153.
[31] L. Zhang, J. Liu, H. Xiao, D. Liu, Y. Qin, H. Wu, H. Li, N. Du, W. Hou, Preparation and properties of mixed metal oxides based layered double hydroxide as anode materials for dye-sensitized solar cell, Chem. Eng. J., 250 (2014) 1-5.
[32] R.M.M.d. Santos, R.G.L. Gonçalves, V.R.L. Constantino, C.V. Santilli, P.D. Borges, J. Tronto, F.G. Pinto, Adsorption of Acid Yellow 42 dye on calcined layered double hydroxide: Effect of time, concentration, pH and temperature, Applied Clay Science, 140 (2017) 132-139.
[33] Y. Zou, X. Wang, F. Wu, S. Yu, Y. Hu, W. Song, Y. Liu, H. Wang, T. Hayat, X. Wang, Controllable Synthesis of Ca-Mg-Al Layered Double Hydroxides and Calcined Layered Double Oxides for the Efficient Removal of U(VI) from Wastewater Solutions, ACS Sustainable Chemistry & Engineering, 5 (2017) 1173-1185.
[34] J. Li, C. Shu, Z. Ran, M. Li, R. Zheng, J. Long, Heteroatom-Induced Electronic Structure Modulation of Vertically Oriented Oxygen Vacancy-Rich NiFe Layered Double Oxide Nanoflakes To Boost Bifunctional Catalytic Activity in Li–O2 Battery, ACS Applied Materials & Interfaces, 11 (2019) 29868-29878.
[35] X.N. Pham, B.M. Nguyen, H.T. Thi, H. Van Doan, Synthesis of Ag-AgBr/Al-MCM-41 nanocomposite and its application in photocatalytic oxidative desulfurization of dibenzothiophene, Advanced Powder Technology, 29 (2018) 1827-1837.

[36] X.N. Pham, M.B. Nguyen, H.S. Ngo, H.V. Doan, Highly efficient photocatalytic oxidative desulfurization of dibenzothiophene with sunlight irradiation using green catalyst of Ag@AgBr/Al-SBA-15 derived from natural halloysite, Journal of Industrial and Engineering Chemistry, 90 (2020) 358-370.

[37] X. Zhang, X. Zhang, X.-G. Wang, Z. Xie, Z. Zhou, NiFe 2 O 4–CNT composite: an efficient electrocatalyst for oxygen evolution reactions in Li–O 2 batteries guided by computations, Journal of Materials Chemistry A, 4 (2016) 9390-9393.

[38] Y. Bi, Z. Cai, D. Zhou, Y. Tian, Q. Zhang, Q. Zhang, Y. Kuang, Y. Li, X. Sun, X. Duan, Understanding the incorporating effect of Co2+/Co3+ in NiFe-layered double hydroxide for electrocatalytic oxygen evolution reaction, Journal of Catalysis, 358 (2018) 100-107.

[39] H. Lv, H. Zhao, T. Cao, L. Qian, Y. Wang, G. Zhao, Efficient degradation of high concentration azo-dye wastewater by heterogeneous Fenton process with iron-based metal-organic framework, Journal of Molecular Catalysis A: Chemical, 400 (2015) 81-89.

[40] G.P. Anipsitakis, D.D. Dionysiou, Radical Generation by the Interaction of Transition Metals with Common Oxidants, Environ. Sci. Technol., 38 (2004) 3705-3712.

[41] X. Chen, Z. Xue, Y. Yao, W. Wang, F. Zhu, C. Hong, Oxidation Degradation of Rhodamine B in Aqueous by UV/$S_2O_8^{2-}$-Treatment System, International Journal of Photoenergy, 2012 (2012) 754691.

[42] C. Liu, D. Pan, X. Tang, M. Hou, Q. Zhou, J. Zhou, Degradation of Rhodamine B by the α-MnO2/Peroxymonosulfate System, Water, Air, Soil Pollut., 227 (2016) 92.

[43] Y. Liu, H. Guo, Y. Zhang, W. Tang, X. Cheng, H. Liu, Activation of peroxymonosulfate by BiVO4 under visible light for degradation of Rhodamine B, Chemical Physics Letters, 653 (2016) 101-107.

[44] R. Wang, S. Su, X. Ren, W. Guo, Polyoxometalate intercalated La-doped NiFe-LDH for efficient removal of tetracycline via peroxymonosulfate activation, Sep. Purif. Technol., 274 (2021) 119113.

[45] J. Zhu, Z. Zhu, H. Zhang, H. Lu, Y. Qiu, Efficient degradation of organic pollutants by peroxymonosulfate activated with MgCuFe-layered double hydroxide, RSC Adv., 9 (2019) 2284-2291.

[46] W. Li, P.-x. Wu, Y. Zhu, Z.-j. Huang, Y.-h. Lu, Y.-w. Li, Z. Dang, N.-w. Zhu, Catalytic degradation of bisphenol A by CoMnAl mixed metal oxides catalyzed peroxymonosulfate: Performance and mechanism, Chem. Eng. J., 279 (2015) 93-102.
[47] B. Liu, W. Song, H. Wu, Y. Xu, Y. Sun, Y. Yu, H. Zheng, S. Wan, Enhanced oxidative degradation of norfloxacin using peroxymonosulfate activated by oily sludge carbon-based nanoparticles CoFe2O4/OSC, Chem. Eng. J., 400 (2020) 125947.
[48] H. Li, Q. Gao, G. Wang, B. Han, K. Xia, C. Zhou, Fabricating yolk–shell structured CoTiO3@Co3O4 nanoreactor via a simple self-template method toward high-performance peroxymonosulfate activation and organic pollutant degradation, Applied Surface Science, 536 (2021) 147787.
[49] S. Guo, H. Wang, W. Yang, H. Fida, L. You, K. Zhou, Scalable synthesis of Ca-doped α-Fe2O3 with abundant oxygen vacancies for enhanced degradation of organic pollutants through peroxymonosulfate activation, Applied Catalysis B: Environmental, 262 (2020) 118250.
[50] Y. Pang, L. Kong, D. Chen, G. Yuvaraja, S. Mehmood, Facilely synthesized cobalt doped hydroxyapatite as hydroxyl promoted peroxymonosulfate activator for degradation of Rhodamine B, J. Hazard. Mater., 384 (2020) 121447.
[51] C. Zhou, Z. Liu, L. Fang, Y. Guo, Y. Feng, M. Yang, Kinetic and Mechanistic Study of Rhodamine B Degradation by H2O2 and Cu/Al2O3/g-C3N4 Composite, Sustainable and Environmental Catalysis, 10 (2020) 317.
[52] M. Zhang, H.-f. Yin, J.-c. Yao, M. Arif, B. Qiu, P.-f. Li, X.-h. Liu, All-solid-state Z-scheme BiOX(Cl, Br)-Au-CdS heterostructure: Photocatalytic activity and degradation pathway, Colloids and Surfaces A: Physicochemical and Engineering Aspects, 602 (2020) 124778.
[53] S.E. More, N. Dwivedi, S. Sable, D.S. Mane, S.R. Tapase, K.M. Kodam, S.V. Bhoraskar, V.L. Mathe, Highly efficient degradation of concentrated Rhodamine-B effluent using environment friendly needle-plate non-thermal plasma probe, Journal of Environmental Chemical Engineering, 8 (2020) 103783.
[54] M.J. Puchana-Rosero, M.A. Adebayo, E.C. Lima, F.M. Machado, P.S. Thue, J.C.P. Vaghetti, C.S. Umpierres, M. Gutterres, Microwave-assisted activated carbon obtained from the sludge of tannery-treatment effluent plant for removal of leather dyes, Colloids and Surfaces A: Physicochemical and Engineering Aspects, 504 (2016) 105-115.

944 [55] Y. Liu, H. Guo, Y. Zhang, X. Cheng, P. Zhou, G. Zhang, J. Wang, P. Tang, T. Ke, W. Li,
945 Heterogeneous activation of persulfate for Rhodamine B degradation with 3D flower sphere-like
946 BiOI/Fe_3O_4 microspheres under visible light irradiation, Sep. Purif. Technol., 192 (2018) 88-98.
947 [56] Y. Chen, J. Yan, D. Ouyang, L. Qian, L. Han, M. Chen, Heterogeneously catalyzed persulfate
948 by CuMgFe layered double oxide for the degradation of phenol, Appl. Catal., A, 538 (2017) 19-
949 26.
950 [57] Q.-T. Sun, B.-D. Xu, J. Yang, T.-T. Qian, H. Jiang, Layered oxides supported Co-Fe bimetal
951 catalyst for carbamazepine degradation via the catalytic activation of peroxymonosulfate, Chem.
952 Eng. J., 400 (2020) 125899.

953